Physics of Fluids

Effects of biomechanical properties of blood on surface tension driven flows in superhydrophilic channels.

Cite as: Physics of Fluids (in press) (2022); https://doi.org/10.1063/5.0088643
Submitted: 19 February 2022 • Accepted: 25 April 2022 • Accepted Manuscript Online: 26 April 2022

Dimitris Pasias, Loukas Koutsokeras, Andreas Passos, et al.

AIP Publishing

Physics of Fluids (in press) (2022); https://doi.org/10.1063/5.0088643 ,

Effects of biomechanical properties of blood on surface tension driven flows in superhydrophilic channels.

D. Pasias[1], L. Koutsokeras[1], A. Passos[1,2], G. Constantinides[1], S. Balabani[2] and E. Kaliviotis[1,a)]

[1]*Dept. of Mechanical Engineering and Material Science and Engineering, Cyprus University of Technology, 45 Kitiou Kyprianou, 3041 Limassol, Cyprus*
[2]*Dept. of Mechanical Engineering, University College London, Roberts Building, Torrington Place, WC1E 7JE London, United Kingdom*
[a)]*Author to whom correspondence should be addressed: e.kaliviotis@cut.ac.cy*

Abstract: Surface tension driven microfluidic flows offer low-cost solutions for blood diagnostics due to the pump-less flow handling. Knowledge of the influence of the biomechanical properties of blood on such flows is key to design such devices, however a systematic examination of that influence is lacking in the literature. We report on the effects of specific haemorheological factors for flows in a superhydrophilic microchannel. Whole human blood and erythrocyte suspensions in phosphate buffer and Dextran solutions were tested. Heat-treated counterparts of the aforementioned samples were produced to alter the deformability of the cells. The flow of the samples was imaged and characterised using micro-Particle Image Velocimetry and tracking techniques to probe the effects of haematocrit, erythrocyte aggregation and deformability. Meniscus velocities, velocity profiles in the channel, and local and bulk shear rates were derived. The mean velocity of blood was affected by the increasing sample viscosity and the reduced erythrocyte deformability as expected. The increased erythrocyte aggregation appeared to affect more the shape of the velocity profiles in the normal, compared to the heat-treated samples. Very high shear rates are observed in the early stages of the flow, suggesting high erythrocyte disaggregation, persisting sufficiently strong until the flow reaches the end of the channel.

Keywords: Blood properties, surface tension, microchannel flow

Nomenclature:

Abbrev. / Symb.	Explanation	Units	Abbrev. / Symb.	Explanation	Units
AR	Aspect ratio (W/h)	-	u	x – direction velocity component	μm s^{-1}
AI	Aggregation index	-	V_{RI}	Velocity ratio	-
DEX	Dextran	-	V_p	Linear velocity (plate flow)	μm s^{-1}
EI	Elongation index	-	V_{ch}	Velocity in the core of the channel	μm s^{-1}
Hct	Hematochrit	-	$\bar{V}_{ch}$	Mean value of V_{ch}	μm s^{-1}
M	M index	-	$\bar{\bar{V}}_{ch}$	Mean value of $\bar{V}_{ch}$	μm s^{-1}
NAB	Non-aggregative blood	-	V_m	Meniscus velocity	μm s^{-1}
O_2	Oxygen	-	$\bar{V}_m$	Mean value of V_m	μm s^{-1}
PBS	Phosphate buffered saline	-	$\bar{\bar{V}}_m$	Mean value of $\bar{V}_m$	μm s^{-1}
PIV	Particle image velocimetry	-	V_{max}	Maximum of V_{ch}	μm s^{-1}
RBC	Red blood cell		w	z – direction velocity component	μm s^{-1}
RBCA	Red blood cell aggregation	-	W	Width of the channel	μm
ROI	Region of interest	-	x*	Normalized x-dir. (x*=x/W)	-
SD	Standard deviation	-	y*	Normalized y-dir. (y*=y/W)	-
$SS_{1/2}$	Half shear stress	-	z*	Normalized x-dir. (z*=z/W)	-
STD	Surface tension driven (flow)	-	$\lvert\dot{\gamma}\rvert$	Shear rate magnitude	s^{-1}
$t_{1/2}$	Half time	-	$\dot{\gamma}_{i-p}$	In plane shear rate component	s^{-1}
TiO_2	Titanium dioxide	-	$\dot{\gamma}_{o-p}$	Out of plane shear rate component	s^{-1}
UV	Ultraviolet	-	ΔP_{Y-L}	Young-Laplace pressure difference	Pa
WB	Whole blood	-	Δt_1	Time period of measurement within the 0 – 16 seconds of the flow	s
h	Half height of channel	μm	Δt_2	Time period of measurement within the 0.64 – 0.8 seconds of the flow	s
h_p	Gap between the plates	μm	Δt_3	Time period of measurement within the 0 – 0.8 seconds of the flow	s
I	Intensity	-	θ_s	Static contact angle	Deg.
k	Power law consistency index	Pa s^n	μ	Dynamic viscosity	mPa s
L_m	Meniscus Position	mm	$\bar{\mu}$	Mean dynamic viscosity	mPa s
n	Power law index	-	$\bar{\bar{\mu}}$	Mean of $\bar{\mu}$	mPa s
r	Radius	μm	μ_{vir}	Virial viscosity	-
P	Pressure	Pa	σ	Surface tension	Nm^{-1}
t	Time	s			

1 Introduction

Microfluidics are increasingly utilised in biomedical research and device development as they offer several advantages regarding sample volume, size and cost effectiveness, automation and disposability[1–5]. Surface tension driven (STD) microfluidic configurations offer simpler and more inexpensive solutions, since they don't require active pumping mechanisms. The flow in a STD microchannel is governed by the surface tension developed in the interface between the working fluid, the air and the channel walls, therefore such flows are highly depended on the surface properties of the material used. Hydrophilic microchannel surfaces favour STD flows, whereas in hydrophophic surfaces no flow is developed.

Blood handling using STD microfluidic platforms has been employed in both research and biomedical diagnostic devices. A number of studies in the literature report on the velocity characteristics of blood in a variety of geometries and configurations. Chang et al.,[6] investigated numerically and experimentally the STD flow of blood in glass and treated (plasma cleaned) PDMS micro channels. Plasma cleaning is necessary to increase the hydrophilicity of the channel, however hydrophobic recovery is an issue, and hence hydrophilic glass chips were also used for the blood tests. The measured blood flow velocity was found to increase with the channel aspect ratio and decrease with increasing fluid viscosity, in agreement with numerical simulations. The upward inclination of the microchannel has been reported to increase blood flow rate, while a downward inclination (angles $< 0^o$) decreases it; this counterintuitive result was attributed to haematocrit effects[7]. Blood flow in open V-groove microchannels has been found to significantly increase, with velocities reaching up to 7.5 cm/s[8]. Additional geometrical characteristics that in general are shown to enhance the STD flow include converging channels[9], channels with protruding pillars [10], channel aspect ratio (AR) up to 1.5[7,11,12].

Spontaneous capillary flow in diverging open channels has also been examined and has been found to have certain limitations[13]: the capillary flow stops when the progressively widened cross section becomes larger than a threshold value, which depends on the geometry and contact angle. Expressions for this limit have been derived for open rectangular channels, and suspended channels (i.e. channels with two opposite walls, having no other boundaries, in which the fluid flows by the surface tension developed on the two opposite walls). Furthermore, in the presence of a sudden expansion, the flow abruptly comes to a halt at this specific location[13]. Berthier et al., [14,15] examined spontaneous capillary flow in curved, open (suspended) microchannels. In this case, contact angles and turn aspect ratio were not found to have any significant effect on the flow (meniscus) profile. However, for rectangular open U-grooved channels, the turning corners were found to affect the flow depending on the radius of the curvature. The capillary flow behaviour was found to be independent of the working fluid as whole blood, tinted water, and IPA solutions all showed similar behaviour. Gosselin *et al.*,[16] investigated the capillary filling of whole blood within a 50μm-radius cylindrical duct made of borosilicate glass. They were able to distinguish the two-phase rheological behaviour of blood by examining the filling distance as a function of time. Until a certain distance blood was found to follow the Newtonian Lucas-Washburn-Rideal (LWR) law, i.e. the flow varies linearly with the square root of time. However, after a few centimetres the flow deviated from the LWR law, as it transited towards a non-Newtonian behaviour. The flow was also examined numerically using the Herschel-Bulkley model in the Navier-Stokes equations showing good agreement with the experiments, and demonstrating the validity of the Herschel-Bulkley model to describe whole blood rheology[16].

Theoretical studies of STD blood flows have demonstrated the effects of the microchannel exit configuration on the flow[17] as well as the effect of the droplet entering the microchannel; the latter has been shown to cause an accelerated flow in the entrance followed by a deceleration downstream[13]. Steady simulations of blood flow in straight and curved tubes using both Newtonian and shear-thinning viscosity models showed that in curved tube flows, the shear-thinning rheology produced blunter axial velocity profiles, decreased secondary flow strengths, and axial vorticity compared to their Newtonian counterparts[18]. It has also been shown, both numerically and analytically, that depending on the strength of the surface forces, capillary ripples of different depths can emerge in the vicinity of the advancing front[19] and that the surface geometrical characteristics can affect the capillary flow[20].

STD microfluidic configurations are also used in Lab-on- a Chip devices for blood plasma separation purposes[21]. Sakamoto *et al.*[22], for example, developed a capillary driven microfluidic device for blood plasma separation and high-throughput screening from a drop of blood. The device is a straight rectangular channel array 2 μm deep, which filters the red blood cells from the whole blood. At the inlet of the device, red blood cells get clogged in the microchannel pillar arrays. In another study, Sneha Maria *et al.* [23] devised a rectangular Polydimethylsiloxane (PDMS) microchannel with filtering hydrophobic patches to detect the glucose levels therein, and Chang *et al.*[24] designed a microchannel with valves to assist in mixing blood with reagents. In more sophisticated approaches, surface tension driven flow of blood has been enhanced by using magnetic liquids to coat the capillary walls to reduce the wall friction[25].

The flow of blood is affected mostly by the erythrocyte concentration (haematocrit), their deformability and the phenomenon of erythrocyte aggregation. The effects of these parameters have been majorly investigated in pressure driven microchannel flows. Lima *et al.*[26–28] studied blood flow in a 100-μm square microchannel for various haematocrits (up to 17%) using a confocal μPIV system, and showed that velocity profiles were markedly parabolic, with fluctuations in the instantaneous velocity profiles related to the increase in the haematocrit. The effect of red blood cell (RBC) aggregation on the flow and structural characteristics of blood in T-type bifurcating microchannels were examined in a series of pressure-driven studies by the authors[29–34]. The bifurcating geometry was found to have a significant effect on the haematocrit (and RBC flux), aggregate size (and aggregate flux), and local viscosity distributions. RBC aggregation affects the bluntness and skewness of the velocity profiles, and impacts on the properties of the cell depleted layer (CDL), which forms adjacent to the channel walls. Recent studies have shown that the CDL is also affected by the design of the utilised syringe pumps[35]. The strong relationship between aggregate size, shear rate and viscosity in aggregated blood microchannel flows has also been illustrated in other works[36–38].

The effect of RBC deformability in microscale flows has also been examined by Passos *et al.*[39] in pressure driven setups for suspensions of healthy and glutaraldehyde-hardened RBCs, perfused through straight microchannels at various hematocrits and flow rates. It was found that in the range of flow rates used the velocity profiles of the hardened cells were sharper than the healthy ones and more Newtonian-like implying a reduction in shear thinning behaviour. The effect of deformability on hematocrit distributions was found to be dependent on the feed hematocrit with the denser suspensions showing stiffened RBCs concentrating more towards the center-line of the 50μm wide channel compared to a healthy case[39]. Czaja *et al.*,[40] also investigated the effect of RBC deformability in the flow by suspending a significant percentage of stiffened RBCs in whole blood. However, no significant difference between stiff and healthy hematocrit profiles was observed. It is believed that this effect is more significant in vessels <50μm.

As illustrated in the above discussion, the mechanical properties of blood are flow dependent, and this need to be considered when designing STD microfluidic configurations. RBC aggregation, for example, is shear rate dependent, and hence the range of flow velocities generated therein is an important factor. The key parameter for flow enhancement in STD flows is the hydrophilicity of the channel surface material, which is quantified by the contact angle. Various methods have been employed in the literature to improve the surface properties of the microchannel materials. Of the most effective treatment techniques are UV and/or oxygen plasma treatment, whereas Titanium dioxide (TiO_2) coating has also a significant effect on hydrophilicity. Oxygen Plasma treatment was found in previous studies to increase hydrophilicity of glass, resulting in better flow conditions in a microfluidic channel[41]. In the Sakamoto *et al.* study[22], the surface wettability was optimized by O_2 plasma irradiation poly-L-lysine (PLL) coating, whereas UV activation is also used to increase wettability[42]. Apart from improving the wettability of the material, the Titanium dioxide coating has also been found to improve hemocompatibility[43]. The benefits of TiO_2 coating have also been illustrated in the study of Kim *et al.*,[44], in which TiO_2 coated glass substrates, with and without O_2 plasma treatment, were tested. Enhanced hydrophilicity occurred when using oxygen plasma treatment and TiO_2 films, compared to bare glass with TiO_2 coating. In addition, the hydrophilicity of the O_2 plasma treated combined with TiO_2 coated glasses was additionally enhanced by UV light irradiation of 10 mW/cm^2 intensity.

Despite the fact that blood STD flows have been examined in the literature, the effect of key properties of blood such as RBC aggregation, deformability and concentration, have not been yet analysed systematically. We recently (Pasias *et al.*,[45]) reported on STD flows of aggregating human blood and other working fluids in a rectangular microchannel, measured by a brightfield μPIV approach. In the present work, we extend this study to systematically examine the effects of blood haematocrit, and red blood cell aggregation and deformability, using an optimised surface treatment protocol to enhance the STD flow. This is of significant importance as a number of pathologies relate to altered states of hematocrit, RBC aggregation and deformability, which the present study attempts to emulate. We use the velocity data to extract information on the magnitude of the local and bulk shearing conditions in STD flows, which relate closely to RBC aggregation, a shear and hematocrit dependent phenomenon, and a key determinant of the non-Newtonian blood rheology. This information will enhance our understanding on the behaviour of such flows, and aid the design of such flows for diagnostic applications. Finally, a heat-treatment approach is used to alter RBC deformability in the present study, which might also shed light on the effect of thermal injuries on the characteristics of blood flow.

2 Methodology

2.1 Sample Preparation and characterization

Samples were acquired with the approval of the Cyprus Bioethics Committee (ref: ΕΕΒΚ/ΕΠ/2016/18), all participants provided informed consent, and all experiments were performed in accordance to the specific guidelines and regulations. Blood was collected into vacuum tubes (BD) preloaded with 1.8 mg/ml EDTA from 10 healthy volunteers. The working fluids tested in the present study were whole blood in its native state (WB), non-aggregative (NAB) and aggregative (Dextran) blood suspensions. The non-aggregative blood samples were prepared by washing RBCs in Phosphate Buffered Saline (PBS), centrifuging at 3600 rpm for 10 minutes (1159g), and re-suspending them in PBS (the procedure was repeated twice). Washed RBCs were suspended in Dextrans (500000-2000000 mw) to produce additional aggregative samples (prefixed as Dex). Different haematocrits (40% and 45%) were produced by adjusting the fluid mediums (PBS or Dex solution) to the RBC volume. Portions of the five aforementioned working fluids (WB, Dex 45%, Dex 40%, NAB 45%, NAB40%) were inserted in a water bath for heat treatment at 50 ^{o}C for 7 minutes, to alter the deformability of the RBCs, similarly to previous studies[46]. Water-milk mixtures at 1:3 proportions were also used as Newtonian fluids (NF) similarly to our previous study[45].

Aggregation and deformability indices were derived utilising Rheoscan-A200 and Rheoscan-D300 instruments respectively. Aggregometry was performed to WB and DEX samples for both normal and heat-treated conditions. The Rheoscan-A200 aggregometer utilises an optical detector to read light transmission intensity (I) as a laser beam is applied on the sample inside the transparent microchip for 120 s. RBCs in the microchip are stirred by a magnetic stirrer for 10s at 900rpm to fully disperse the RBC aggregates. The light transmission is affected by the aggregation of RBCs, resulting in a time-dependent intensity curve I(t). The curves for each sample type were averaged (all donors) and a mean light transmission intensity ($\bar{\mathrm{I}}$) curve was produced as shown in Figure 1a.

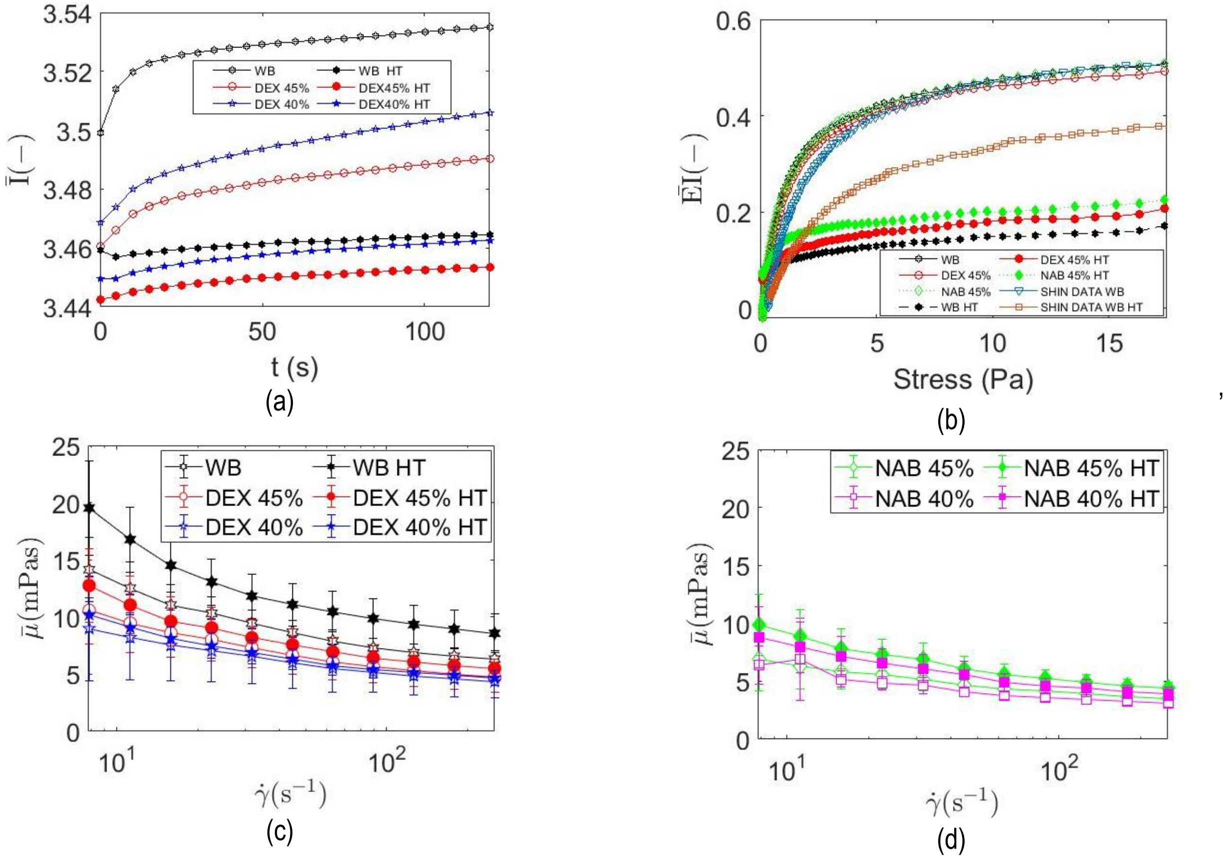

(a)

(b)

,

(c)

(d)

Figure 1. (a) Mean aggregation intensity (all donors) over time for normal WB, DEX45%, DEX40% and the heat-treated counterpart samples. (b) Mean Elongation index $\overline{\mathrm{EI}}$ for WB, DEX45%, NAB45% for normal and heat-treated samples, and EI results for WB and WB HT from Shin *et al.* [46]. Mean viscosity $\bar{\mu}$ for the aggregative (panel c) and non-aggregative (panel d) samples, at shear rates between from 251.2 to 7.785 s^{-1}.

The I(t) curves were further analysed to produce the aggregation index AI[47], as the ratio of the area under the curve to the total area (above and below the curve) for 120 s. AI was obtained at each experiment for each working fluid, and then averaged accordingly, for all donors, to find a mean aggregation index ($\overline{AI}$).

Deformability measurements were performed for the WB and DEX45% and NAB45% samples, and for their heat-treated counterpart cases expressed in terms of the Elongation index, EI, defined as $EI = \frac{A-B}{A+B}$ (A and B are the length and the width of the laser diffraction pattern created by the deformed RBCs) [48]. The same procedure as with the aggregation intensity curves was followed to produce the mean $\overline{EI}$ curves over shear stress (Figure 1b). For a clearer presentation the curves in Figure 1 error bars are not included. However, the average standard deviation in the steady state part of each $\overline{EI}$ curve has been evaluated for each case, and it was found to be less than 4% of the $\overline{EI}$ values (3.44% in the DEX45% case).

Viscosity measurements were performed using a Brookfield DVIIT instrument, utilising a cone-plate geometry. Samples were loaded in the plate of the viscometer with a micropipette (0.6 ml volume) and tests were initiated approximately 30 seconds afterwards. Viscosities were measured by ramping down shear rates from 251.2 s^{-1}, to ensure RBC aggregate dispersion, to 7.785 s^{-1} (30 seconds measurement time at each shearing point), without pre-shearing between shear points. The aforementioned shear rate points (251.2, 7.785 s^{-1} including 15.82 s^{-1}) were selected for the development of relevant viscosity indices. The maximum shear stress that cells were exposed at the highest shear rate was approximately 1.5 Pa for 30 seconds, hence much lower from stress/duration causing membrane damage and haemolysis[49]. The duration of a complete viscosity test was ~8.5 minutes, and the viscosity measurements were performed at the end of the shearing period at each point. All measurements were performed at room temperature (25 ± 0.5 ^{o}C). A mean viscosity $\bar{\mu}$ was calculated at each shear rate from all tests (n=10) for each sample type, and shown in Figure 1c and d, with the error bars indicating the standard deviation.

From the mean viscosity $\bar{\mu}$ data, the virial viscosity index (μ_{vir}), was calculated similarly to another study[50], to examine the extent of shear thinning behaviour of the working fluids:

$$\mu_{\mathrm{vir}} = \frac{\bar{\mu}(\text{at } \dot{\gamma}=7.88 \text{ or } \dot{\gamma}=15.82\ ) - \bar{\mu}\ (\text{at } \dot{\gamma}=251.2)}{\bar{\mu}\ (\text{at } \dot{\gamma}=251.2)} \qquad [1]$$

The viscosity values $\bar{\mu}$ were also averaged in the shear rate range 251.2 s^{-1} to 7.785s^{-1}, to produce the index $\bar{\bar{\mu}}$, which could assist in the analysis of the results.

2.2 *Channel surface treatment*

Microscope glass slides (Superfrost 26x76mm) were used for the microchannel construction, due to the intrinsic hydrophilic properties of glass. Prior to TiO_2 treatment the slides were cleaned according to the following cleaning protocol: firstly, the slides were rinsed with distilled water, then immersed for 30 mins in hydrochloric acid/distilled water (HCL/DI) solution in 1:2 ratio, followed by a final rinse with DI water. UV/ozone and Plasma treatment was also performed to the cleaned glasses for different treatment times to assess their effect on improving glass wettability. UV/ozone was applied for 10, 20 and 30 minutes using Ossila E511 UV/ozone cleaner apparatus. Plasma treatment of the microscope glasses has been performed in a homemade apparatus based on a modified microwave oven and a standard 500ml glass bottle. The glass bottle has been converted into a small vacuum chamber by connecting it to a dry-scroll vacuum pump (Agilent, Triscroll) via a custom-made Teflon cap through the walls of the microwave oven. The glass slides were placed into the glass bottle which was sealed and then evacuated to a lower pressure, in the order of $1 \times 10^{-1}\mathrm{Torr}$. The microwave power selector was at the highest setting and the built-in timer was used to control the treatment time. By turning on the microwave power, a vivid plasma was created in the whole bottle volume, having a red-purple colour, indicating that air was the main gas in the bottle. The glasses were treated with Plasma for 5, 10, 20 and 30 seconds.

The static contact angle measurements were performed by capturing deionised water drop images, using a contact angle measurement set-up, which consisted of a USB camera, aligned with the surface plane of the specimen similar to our previous work[45]. Prior to any treatment the contact angle was measured to be approximately 45^{o}. UV and plasma treatment resulted in a significant reduction (up to ~10^{o}), however a loss in hydrophilicity was observed after several hours, when the contact angle increased to more than ~20 ^{o}. Plasma treatment of 5s and 10s had the smallest contact angles compared to 10s and 30s treatment.

$Ti0_2$ coating was applied on the pre-cleaned glasses with two methods. The first method was by using a standard compression spray gun for spray coating similar to another study[51]. The second method was spin coating as in another study [52] at 3000rpm for 1 minute and then left to dry at room temperature for 5 minutes. The fluid used in spaying and coating was Sufashield G ($Ti0_2$ nano particles suspended in water). Both methods resulted in similar contacts angles. $Ti0_2$ treatment was also performed after plasma treatment for 10s on the pre-cleaned glasses, however UV treatment was not performed since plasma 10s was shown to be more effective. The results of Plasma, TiO_2 treatment, and their combination is compared in Figure 2a. Pre-cleaned glasses treated in combination with Plasma for 10s and TiO_2 coating provide lower contact angles than plasma or TiO_2 coating alone; hence this method was chosen to be the final treatment of the glasses.

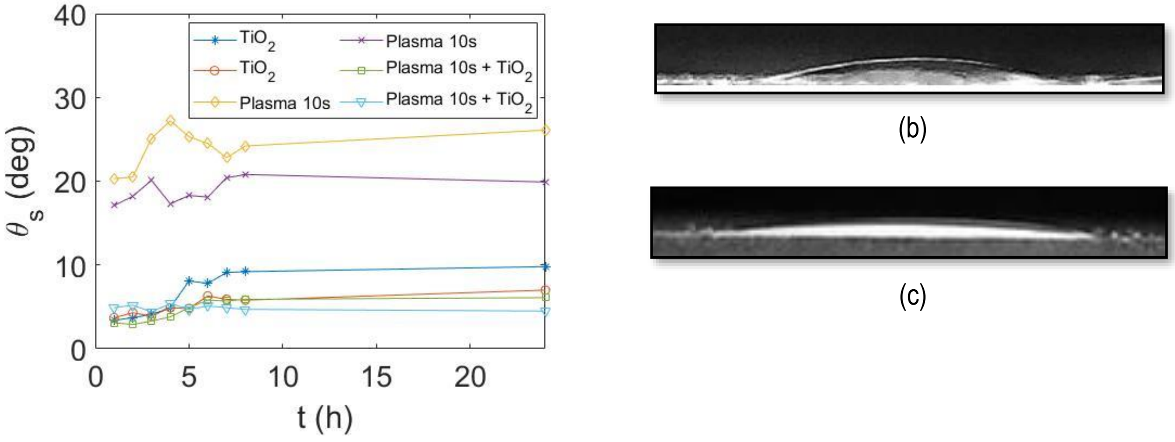

(b)

(c)

(a)

Figure 2. Contact angles of deionised water on UV, Plasma, and $Ti0_2$ treated microscope glasses vs time. (a) Contact angle, θ_s, for TiO_2, Plasma for 10s and their combination. Drop of distilled water on a UV only treated surface (b), and a fully treated surface (c).

2.3 *Microfluidic channel fabrication.*

A converging geometry (3 degrees) was adopted for the design of the microchannel, as it has been shown that this configuration has a favourable effect on the flow[9,10]. The micro channel used in the experiments was made of glass slides (Superfrost, 1mm thickness) and double-sided tape (Tessa, ~100μm height) as shown in Figure 3. The design included a round deposition well, the converging geometry part, and a straight section leading to the exit hole. Figure 3 also shows the schematic of the complete experimental setup, comprising of the microscope/cameras arrangement. The adhesive tape was cut according to design using xurography techniques[53], using a commercial Silhouette Portrait 2 cutter. The converging section had a width of 5 mm at the beginning of the channel, and a length of 20 mm until it converged to a width of ~1mm. The top slide was drilled at the beginning and at the end of the channel creating the deposition well and the exit of the channel.

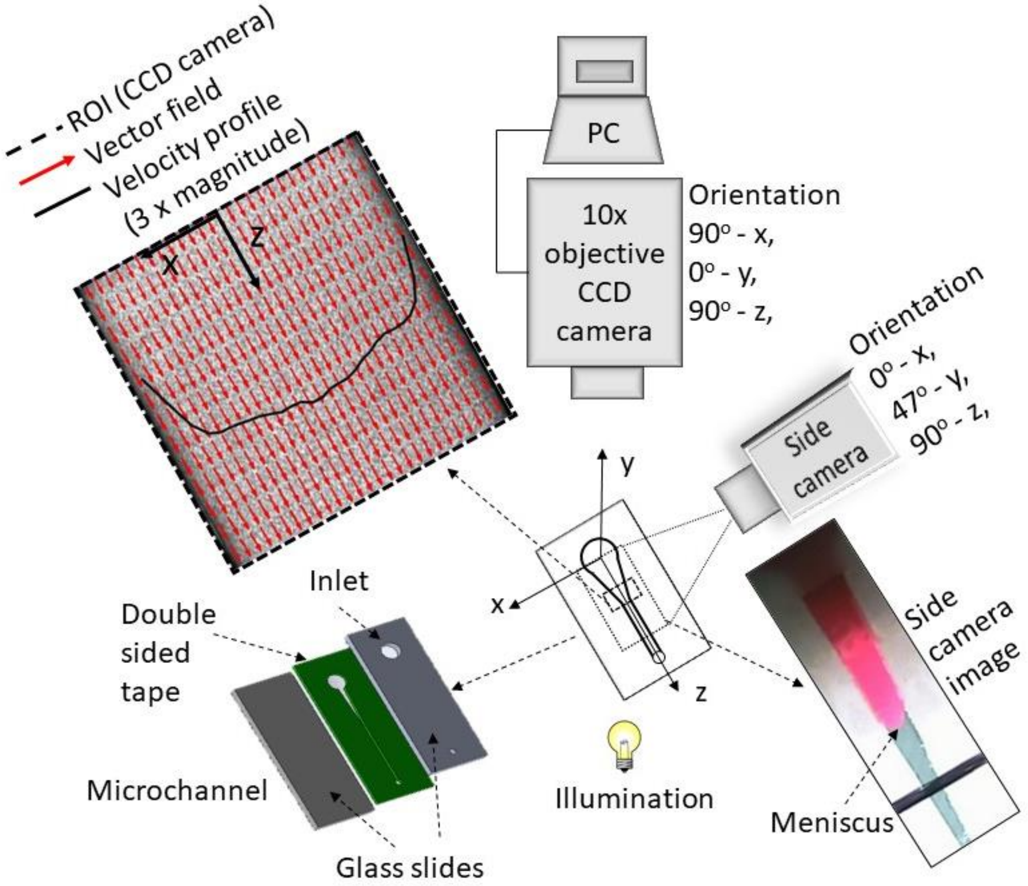

Figure 3. Annotated schematic of the capillary driven micro channel flow, and the PIV measurement set up: the width (W) and depth (h) of the channel were W = 5mm at the entrance converging to ~1 mm at the end of the converging section and h ~ 100µm, respectively (diagrams and region of interest not to scale).

2.4 Experimental setup

The experimental setup, shown schematically in Figure 3, is similar to that in our previous study[45] with the addition of a side camera to capture the meniscus flow. The micro channel was placed horizontally on the microscope stage A 25µl drop of fluid was placed at the entrance, using a micropipette and the fluid was then set in motion through the channel by capillary forces. The flow was recorded with a CMOS camera (IDT X3, 2000 images were captured at 1250 fps) attached on the microscope (upright BX51 OLYMPUS, 10X-objective, NA=0.25) and images were analysed using Matlab. The spatial resolution of this optical setup was 1.65 µm/pixel. The side camera (JVC TK-C1380 colour, with a 60mm Panasonic lens) was fixed at the maximum angle possible (47° to the y-axis) to capture the meniscus on the horizontal plane.

2.5 Micro-Particle Image Velocimetry processing

The acquired flow images were processed using Matlab PIVLab software to resolve the velocity field, and to analyse /plot the velocity profile in the channel (Figure 3). RBC were used as tracing particles similar to our previous work[45]. Three passes with interrogation windows (IW) of height and width of 32, 16 and 8 were used for the µPIV processing of the acquired images. In the present study, a 13.2 µm vector spacing (for 10 X magnifications) was achieved. Velocity profiles were calculated by axially averaging all of the velocity vectors in a region of interest (ROI) in the channel after the meniscus had progressed. The choice for averaging the velocity vectors in the channel, and not the z-component of velocity only, was based on the fact that the convergent geometry resulted in a negligible increase of the cross-flow velocity components. In addition, of particular importance in the present work is the magnitude of the shear strain rate, which is calculated including an estimation of the out-of-plane shear component. The latter is calculated using the maximum velocity of the profile and the channel height (a detailed description is provided in a later section).

2.6 Meniscus velocity calculation

After the sample deposition and the initiation of the flow, the meniscus position was recorded with the side USB JVC colour camera (Figure 3) at a frame rate of approximately 20 fps. The data were analysed to track the position at each frame using a tracker software package (https://www.rollapp.com/app/tracker). For the calculation of the mean meniscus velocity $\bar{V}_m$, the following method was utilised. First, the tracked time-dependent meniscus location (L_m) was fitted using a power law equation $\mathrm{L_m} = Ct^n$ (R-square close to 1, C and *n* are constants) (Figure 4). The meniscus velocity as a function of time was derived by differentiating the position function, $V_m = \frac{dL_m}{dt} = Cnt^{n-1}$, for all tests (n=10) and for the different samples. The mean meniscus velocity $\bar{V}_m$ for each sample type was calculated as the average of V_m from all donors (n=10). For example, Figure 3b illustrates the V_m curves from all donors, and the calculated of $\bar{V}_m$ for the WB sample case. In addition, an average velocity, $\bar{\bar{V}}_m$, was calculated as a time-average within different time periods.

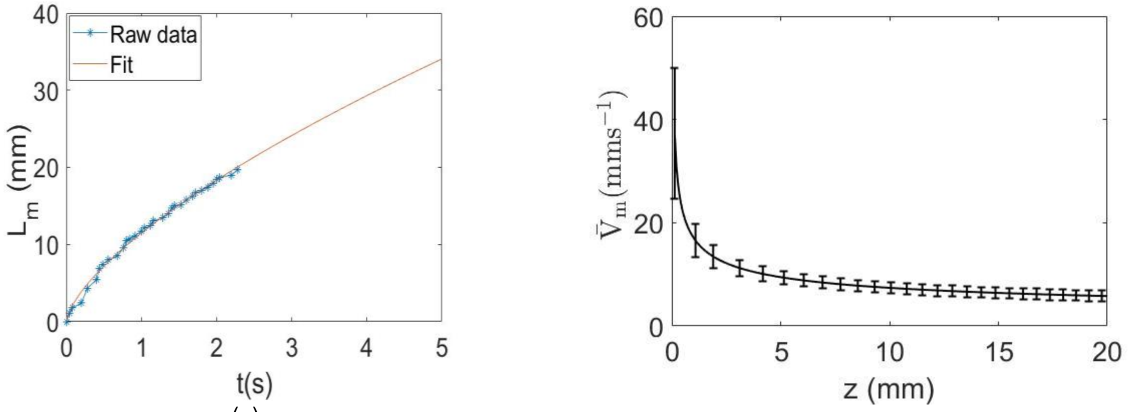

(a)

(b)

Figure 4. a) Raw data of the meniscus position in time from a representative sample of WB (symbols) with the fitted power law function L_m. b) Mean meniscus velocity $\bar{V}_m$, for the WB samples (n=10), calculated as the average from each sample, using equation $V_m = \frac{dL_m}{dt} = Cnt^{n-1}$ (parameters C and n derived from the L_m fitting).

2.7 Velocity profiles

Velocity profiles, $\bar{V}_{ch}$, were extracted from the measured μPIV velocity vectors (see Figure 3 for a representative vector field). First the instantaneous velocity profiles, V_{ch}, were derived, which were extracted in the core of the flow, after the meniscus has passed the field of view. V_{ch} was calculated from averaging the velocity vectors within the region of interest in the direction of the flow. Further, V_{ch} was averaged in time to produce $\bar{V}_{ch}$, the ensemble-averaged velocity profile for the different time periods (Δt_1 = 0 - 0.16s, Δt_2 = 0.64 - 0.8s, and Δt_3 =0 - 0.8s). An average channel flow velocity, $\bar{\bar{V}}_{ch}$, was calculated from the velocity profiles $\bar{V}_{ch}$, from all repetitions in each sample category as follows (n=number of samples):

$$\bar{\bar{V}}_{ch} = \frac{1}{n}\sum_1^n\left[\frac{1}{x^*}\int_{-0.5}^{0.5}\bar{V}_{ch-n}\,dx^*\right] \qquad [2]$$

Indeed, examining the velocity components u and w (produced by the microPIV technique for the x and z directions of the flow respectively), revealed that the magnitude of the transverse velocity component u was < 1% of the maximum value of the axial velocity w component.

The region of interest used for the micro PIV analysis was rectangular, and was selected to cover the entire channel (see the inset in Figure 3). Therefore, the flow analysis domain included a small portion of the walls, in which zero blood velocity was expected to appear. Due to refraction effects at the walls the first line of vectors near the end of the vector field was neglected, so the field was reduced by 13.2 μm in each side. Therefore, the portion of the vector field affected by the zero velocities due to the wall, was significantly minimised.

For presentation and comparison purposes the x-coordinate in each mean velocity profile was normalized with its width, so that

$-0.5 \leq x^* \leq 0.5$. Due to small variations in the dimensions between the constructed microchannels, velocity points could appear at slightly different x* positions in the V_{ch} profiles. Therefore, to minimize errors when averaging the V_{ch} profiles to produce the mean $\bar{V}_{ch}$ velocity, the position of the velocity points from the centreline were used rather than x*.

2.8 Shearing rates

RBC aggregation is a shear and time dependent phenomenon and therefore it is important to estimate the shearing conditions generated by the STD flows under investigation, particularly when the in situ/channel aggregation is the focus of the investigation. The shear rate magnitude in the microchannel was evaluated from the individual shear strain components as in other studies[45,54], assuming that the u and v velocity components are negligible and that the flow is fully developed ($\frac{\partial}{\partial w} = 0$):

$$|\dot{\gamma}| = [\left(\frac{\partial w}{\partial x}\right)^2 + \left(\frac{\partial w}{\partial y}\right)^2]^{\frac{1}{2}} \qquad [3]$$

The first term (the in-plane shear rate component) can be calculated from the experimental velocity profile as follows; $\dot{\gamma}_{i-p} = \frac{\partial w}{\partial x} = \frac{d\bar{V}_{ch}}{dx}$. The out-of-plane shear rate component ($\dot{\gamma}_{o-p} = \frac{\partial w}{\partial y}$) was estimated as $\frac{\bar{V}_{ch\,max}}{h}$ where $\bar{V}_{ch\,max}$ is the maximum velocity in the experimental velocity profile ($\bar{V}_{ch}$) and h the channel height (h=100μm). Therefore $\bar{\dot{\gamma}}_{ch}$ was obtained as

$$\bar{\dot{\gamma}}_{ch}(x^*) = \sqrt{(\frac{d\bar{V}_{ch}}{dx})^2 + (\frac{\bar{V}_{ch\,max}}{h})^2} \qquad [4]$$

An average shear rate in the channel flow, $\bar{\bar{\dot{\gamma}}}_{ch}$, was obtained by integrating $\bar{\dot{\gamma}}_{ch}(x^*)$ in the x^* and dividing by Δx^*:

$$\bar{\bar{\dot{\gamma}}}_{ch}\,(x^*) = \frac{1}{\Delta x^*}\int_{-0.5}^{0.5} \bar{\dot{\gamma}}_{ch}\ dx^* \qquad [5]$$

A nominal rate of shear could also be obtained by utilizing the meniscus velocities (Figure 4), as $\bar{\dot{\gamma}}_m(z) = \frac{\bar{V}_m(z)}{h}$, and another bulk shearing parameter was calculated from the meniscus velocity as the mean of the $\bar{\dot{\gamma}}_m(z)$ data: $\bar{\bar{\dot{\gamma}}}_m = \frac{\sum_1^n \bar{\dot{\gamma}}_m(z)}{n}$, to indicate the overall shear strain that the fluid is exposed to throughout the duration of the surface driven flow.

2.9 Uncertainty and error sources

In brightfield μPIV techniques, due to the large depth of correlation of the microscope objective, a certain degree of error occurs[45]. This finite depth of correlation leads to an underestimation of the velocity magnitude, the extent of which was assessed in the present study and agrees with previous reports[45,55,56]. However, the velocity underestimation is found to be consistent across the largest part of the flow field (please see Figure S1a in the supplementary material) and therefore the shape of the velocity profile should be qualitatively preserved. In addition, the comparison of channel and meniscus velocities shown in Figure S1b provide evidence for the relatively good validity of the velocity measurements.

The side walls of the channel are constructed by a double-sided adhesive tape, which introduces an apparent roughness on the side wall-flow interface. In addition, due to small variations in the dimensions between the constructed microchannels, velocity points could appear at slightly different x* positions in the V_{ch} profiles. Therefore, to account for this V_{ch} profiles were averaged by considering the velocity values according to their position from the centreline, to produce the mean $\bar{V}_{ch}$ velocity profile.

The sample deposition at the entrance of the channel is conducted with great care by the trained operator using a micropipette. The sample volume is consistently controlled using the micropipette, however, uncertainties due to sample handling might be possible. In the present work, cases showing abnormal behaviour (specially in channel and meniscus velocity due to side walls having small air bubbles hence blood flowing through the side walls), have been excluded from the analysis. Viscosity values at the lowest shear rate (12.5 s^{-1}) were close to the lower sensitivity limit of the viscometer (accepted at the 5% of the transducer torque range).

The heat treatment, as a condition, is relevant to various pathological states, e.g. thermal injuries or heat-stroke[57], and it is of interest from this point of view also. Heat-treating the samples however, is known to have a slight effect on the optical properties of blood[58], which may affect slightly the RBC aggregation and PIV velocity results. The Dextran suspending medium is expected also to have been affected by the heat treatment. More specifically, the stability of Dextran is decreased with increasing temperature, since thermal degradation increases at higher temperatures. However, the initial decomposition temperature (T_i) for dextran occurs at T_i ~283°C, hence at 50°C which dextran was heated in these experiments no thermal degradation is expected[59]. In addition, the intrinsic viscosity of Dextran (which is also depended on the solvent medium - water in this study) reduce with increasing solution temperature[60]. The intrinsic viscosity of Dextran2000000 with water as solvent, which was used in this work, is expected to have been decreased by ~27% by heating from room temperature ~25 °C prior to heat treatment to ~50 °C post heating[60].

3 Results

3.1 Rheological and structural characteristics of the samples

The rheological properties of blood are mainly influenced by RBC aggregation (RBCA), deformability, haematocrit, and plasma viscosity. The characteristic indices for the aforementioned quantities are given in Figure 5 to assist the discussion and analysis of the results thereafter.

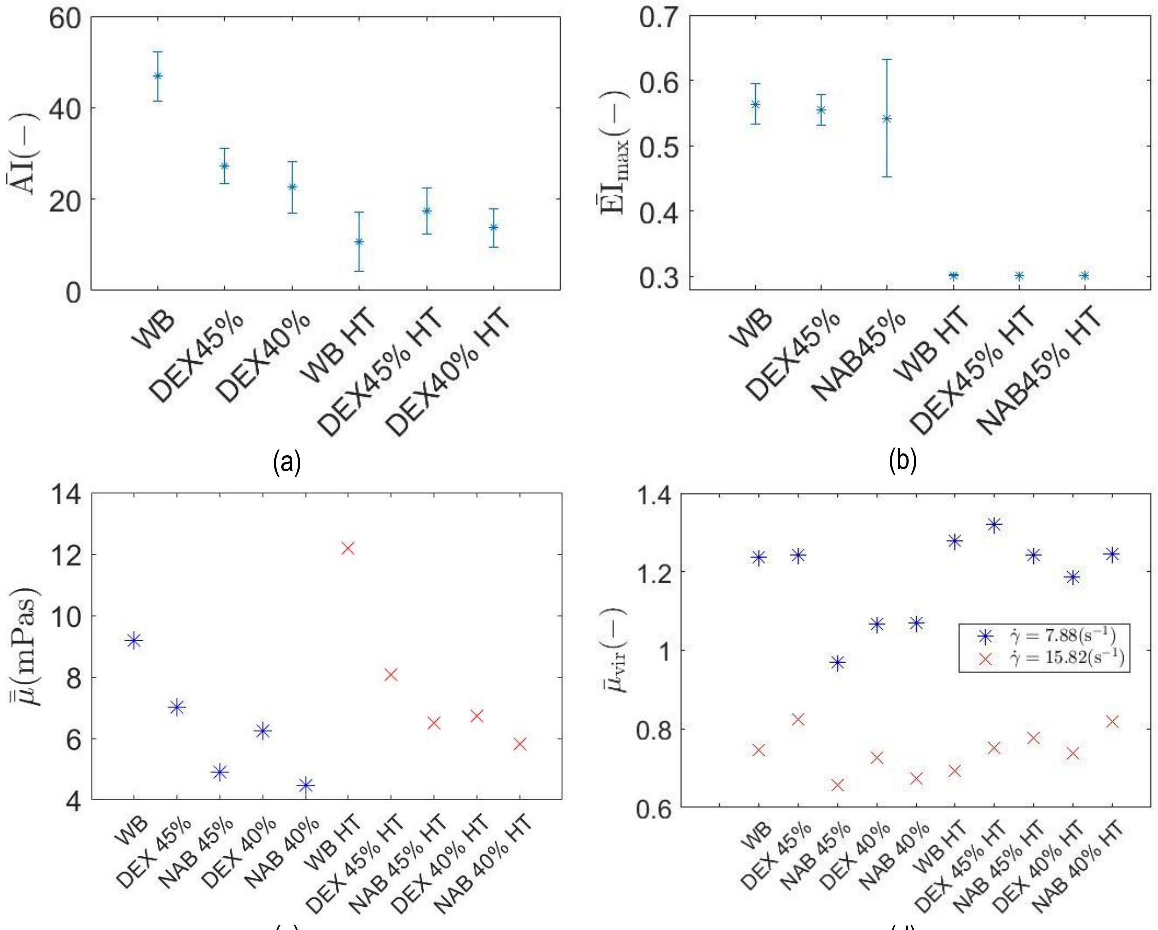

(a) (b)

(c) (d)

Figure 5. (a) Aggregation index $\overline{\mathrm{AI}}$ for WB and Dextran working fluids, and from all donors. $\overline{\mathrm{EI}}$ for all working fluids shown in panel (b). (c) Bulk viscosity index $\bar{\bar{\mu}}$, and (d) the virial viscosity index $\bar{\mu}_{\mathrm{vir}}$ at shear rates $\dot{\gamma}$=7.88s^{-1} and $\dot{\gamma}$=15.82s^{-1}.

Figure 5a shows the averaged aggregation indices ($\overline{\mathrm{AI}}$) derived from the curves of Figure 1a. Both Figure 1a and 5a, demonstrate that RBCA is higher in whole blood than in Dex45% and Dex40% for both heated-treated and normal samples. The higher aggregation tendency in WB, compared to DEX45% and DEX40%, is expected since the dextran concentration employed is relatively low to moderate in terms of influence in RBCA [61]. RBCA in Dex45% is higher than Dex40% as expected, due to the higher haematocrit[62]. The heat treatment has an obvious effect on RBCA, suppressing the phenomenon, however the decrease does not appear systematic. It can be seen that both Dextran samples exhibit the same change in aggregation post heat treatment whereas WB shows a more pronounced decrease in AI; this can be probably attributed to the heat-treatment also affecting the plasma proteins responsible for the RBCA phenomenon to a greater extent than the Dextran molecules. According to Lerche *et al.*,[63] the bridging energy of Dextran molecules (4g% of D70 in that study) is higher than that of fibrinogen found in normal plasma, and therefore an increased rigidity of RBCs, or/and a heat-altered macromolecule-glycocalyx interaction can have a greater impact in the case of WB compared to Dextran samples.

The measured RBC deformability index ($\overline{\mathrm{EI}}$) of the samples are shown in Figure 5b. The maximum elongation index ($\overline{\mathrm{EI}}_{\mathrm{max}}$) is approximately the same for all three normal (pre-heat) working fluids tested (both aggregative and non-aggregative), indicating that suspending the cells in PBS or Dextran to induce aggregation does not have a significant impact on cell deformation. The heat-treatment, however, reduce significantly the elongation index for all working fluids tested as observed in Figure 5b; all working fluids exhibit the same EI following heat-treatment and hence the $\overline{\mathrm{EI}}_{\mathrm{max}}$ percent difference is almost the same for all working fluids. Higher viscosity is observed at conditions of high aggregation, and hence higher shear stresses need to be applied for cell deformation.

In terms of the mean viscosity behaviour, as shown in Figure 5d, the aggregative samples have higher $\bar{\mu}$ than the non-aggregative ones, which agrees with other studies[64]. The same applies for the heat-treated (HT) working fluids, however their non-Newtonian behaviour seems not significantly affected, as indicated by the virial viscosity $\bar{\mu}_{vir}$ index (Figure 5d). That is the $\bar{\mu}_{vir}$ for the HT samples is similar to that of the normal WB and Dex45% samples, even though the aggregation and deformability of the RBCs has been reduced in the HT cases. Indeed, since RBC deformability (Figure 5b) and aggregation, (Figure 5a) have been reduced post HT, the shear thinning behaviour would be expected to be less obvious. However, RBC aggregation and deformability are still not negligible: there is a ~37% reduction in AI for the Dex cases (and a larger reduction of ~77% in the WB case) and ~ 45% reduction in the deformability of the RBCs ($\overline{\mathrm{EI}}_{\mathrm{max}}$ index). Furthermore, it has been reported in the literature[46], that when the deformability of RBCs is reduced by heat treatment, the disaggregating shear stress (i.e. the minimum shear-stress required to disperse the aggregates) is increased, depending on the concentration of the aggregating factor (fibrinogen in that case). Increased disaggregating shear stress (DSS) implies both increased viscosity, and non-Newtonian behaviour of the fluids [65]. Another cause of the high viscosity and persisting non-Newtonian behaviour of the HT samples, might be the tumbling of red blood cells in the flow instead of the less energy demanding rolling motion[66]. It is therefore apparent, that the loss of deformability balances out the effect of reduced AI, and hence the samples retain their shear thinning behaviour.

3.2 Meniscus velocity

Figures 6a, and b show the mean meniscus velocities $\bar{V}_m$ along the axial direction for all working fluids, while Figure 6c an average velocity value $\bar{\bar{V}}_m$ calculated from z=5 mm to 20mm, i.e. excluding the non-linear decelerating part of the flow to facilitate comparisons. The velocity data in Figure 6b in conjunction with the aggregation tendency of the tested working fluids shown in Figures 1 and 5 indicate that the more aggregative the sample is, the lower the meniscus velocity. The heat-treated samples also exhibit lower mean meniscus velocity $\bar{\bar{V}}_m$ (Figure 6c) compared to normal non heat-treated ones probably due to the increased viscosity ($\bar{\mu}$).

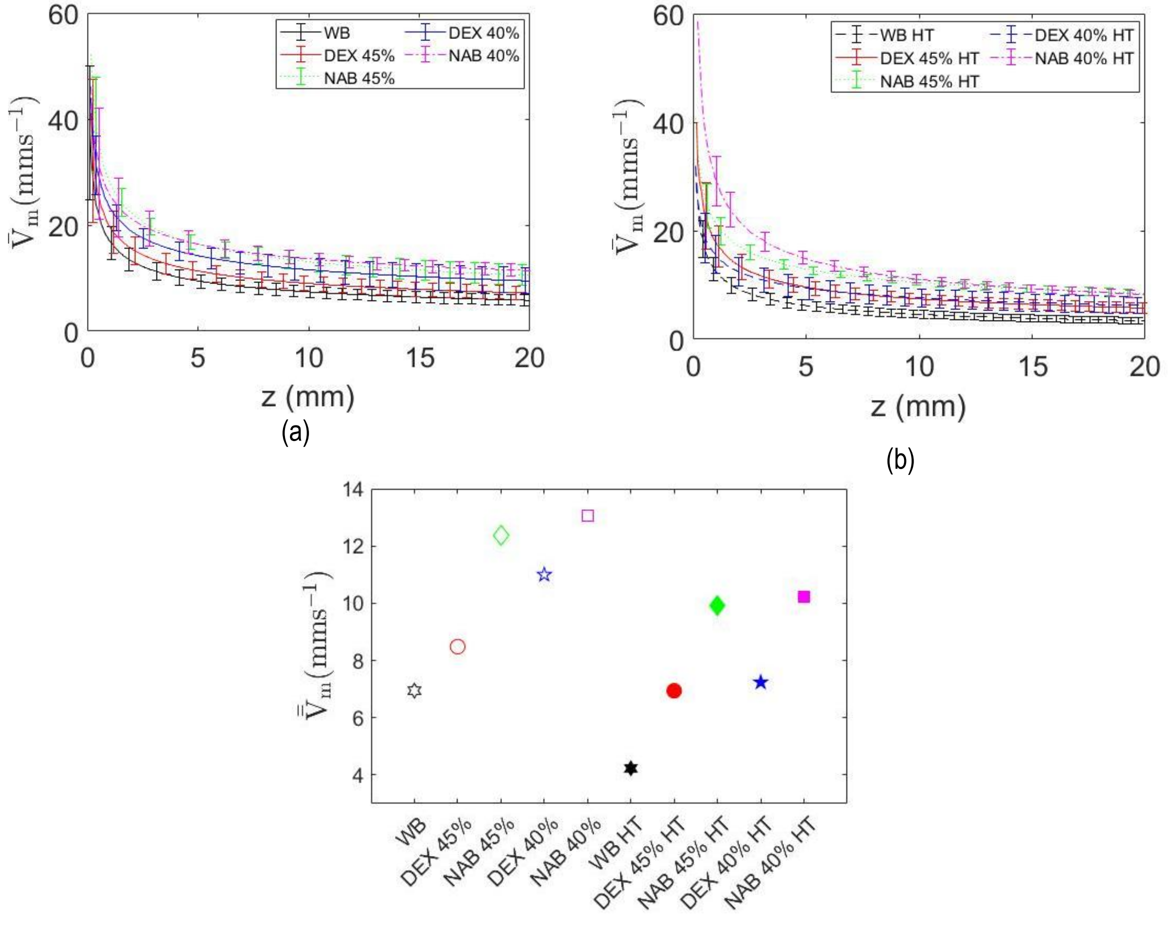

(a)

(b)

(c)

Figure 6. (a) Meniscus velocity, $\overline{\mathrm{V}}_{\mathrm{m}}$, from all non heat-treated samples tested. b) Meniscus velocity, $\overline{\mathrm{V}}_{\mathrm{m}}$, from all heat-treated samples tested. c) Average meniscus velocity, $\overline{\overline{\mathrm{V}}}_{\mathrm{m}}$, of all working fluids from z=5mm until end of the channel (z=20mm)

3.3 Velocity profiles

The channel velocity profiles $\left(\overline{\mathrm{V}}_{\mathrm{ch}} \text{ and } \overline{\overline{\mathrm{V}}}_{\mathrm{ch}}\right)$ shown in Figure 7 demonstrate the role of RBC aggregation similarly to the meniscus velocities ($\overline{\mathrm{V}}_{\mathrm{m}}$ and $\overline{\overline{\mathrm{V}}}_{\mathrm{m}}$ in Figure 6). This is apparent when comparing the DEX 45% to NAB 40% sample and is attributed to the elevated viscosity found in the DEX samples (Figure 6c). The decelerating behaviour of the meniscus velocity is also apparent in Figures 7e and 7f comparing $\overline{\mathrm{V}}_{\mathrm{ch}}$ and $\overline{\overline{\mathrm{V}}}_{\mathrm{ch}}$ at different periods Δt_1, and Δt_2. The velocity values are lower in the Δt_2 period, in agreement with the plots in Figure 6a. The impact of the reduced RBC deformability is also evident in the reduced velocity profiles of the heat-treated samples in Figure 7b and d. Heat-treated samples exhibit smaller differences in channel velocities (the minimum velocity is within approximately 30% of the highest velocity) compared to normal ones; however, the standard deviation between samples appears much higher, and no statistically significant differences can be detected between samples. Figure 7a and 7c indicate significant differences in channel velocities between samples, with the velocity of the NAB40% appearing higher than the other cases. The maximum velocity of WB samples appears at the lower end of the velocities observed in both Δt_1, and Δt_2 periods of measurement, and the same applies for the heat-treated counterparts.

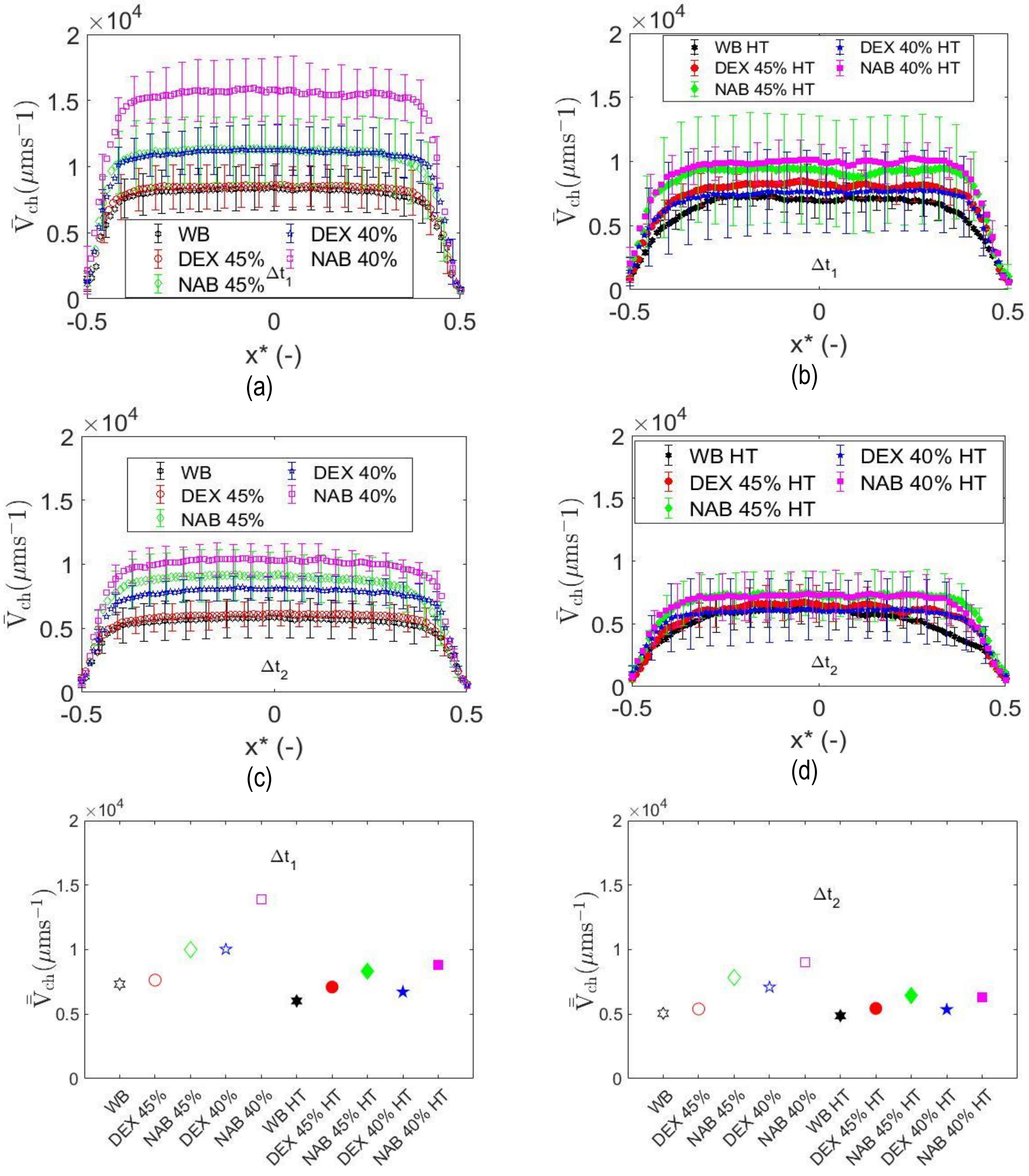

(a) (b) (c) (d) (e) (f)

Figure 7. (a) and (b): $\overline{\mathrm{V}}_{\mathrm{ch}}$ at Δt₁ for normal and HT samples respectively. (c) and (d): $\overline{\mathrm{V}}_{\mathrm{ch}}$ at Δt₂ for normal and HT samples respectively. $\overline{\overline{\mathrm{V}}}_{\mathrm{ch}}$ at Δt₁ and Δt₂ are shown in (e) and (f).

The same trends are observed in the velocity characteristics measured for the overall period Δt_3 (not shown here). Another important characteristic of the velocity field, is the shape of the velocity profiles. It appears from Figure 7 that the heat-treated samples show a slightly smaller flat area in their profile, compared to the normal samples, which could imply a higher maximum to mean velocity ratio. To quantify these characteristics a velocity ratio index was defined, similar to previous studies [30,31,39], which could allow assessing also the effects of aggregation and RBC deformability: $\mathrm{V}_{\mathrm{RI}} = \frac{\overline{\overline{\mathrm{V}}}_{\mathrm{ch}}}{\overline{\mathrm{V}}_{\mathrm{ch-max}}}$. The maximum velocity $\overline{\mathrm{V}}_{\mathrm{ch-max}}$ was utilised for the normalization of the mean channel velocity. Hence, V_{RI} will be closer to a value of 1 when larger population of RBCs approaching the maximum velocity in the channel. The resulted V_{RI} indices calculated for the overall period Δt_3 are shown in Table 1. V_{RI} was found to be slightly decreased in the HT samples, particularly for WB and aggregative samples; comparing WB, DEX45% and DEX40% shows that the higher the aggregation the largest the reduction in velocity ratio. This is more obvious in Figure 8, which also illustrates the effect of haematocrit: the higher the haematocrit, the greater the effect of HT on the bluntness of the profiles. Non-aggregative samples NAB45% and NAB40% exhibit a much smaller decrease in V_{RI} compared to aggregative ones. However, although a decrease in velocity ratio is observed post HT, for both aggregative and non-aggregative samples, the change is not statistically significant.

Sample	WB	WB HT	Dex 45%	Dex 45% HT	NAB 45%	NAB 45% HT	DEX 40%	DEX 40% HT	NAB 40%	NAB 40% HT
V_{RI} (-)	0.87	0.80	0.86	0.83	0.87	0.87	0.88	0.87	0.86	0.86
ΔV_{RI}%	-8.50		-1.06		-0.13		-0.75		-0.52	

Table 1. V_{RI} calculated for the Δt_3 period, for all samples and conditions. The difference between the normal and the HT cases are also shown.

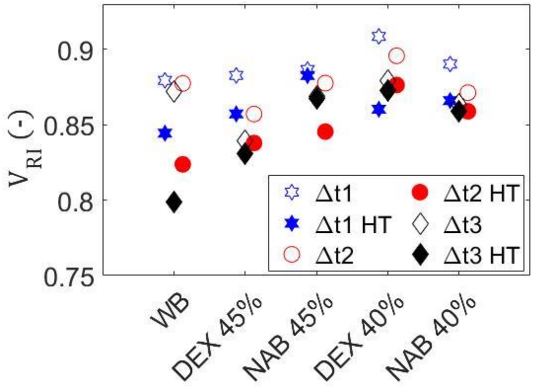

Figure 8. Comparison of V_{RI} between all samples, conditions and periods of time.

3.4 *Shearing conditions*

Figure 9 shows the $\bar{\dot{\gamma}}_{ch}$ profiles obtained for all cases and for the two measuring periods Δt_1, and Δt_2. From the $\bar{\dot{\gamma}}_{ch}$ profiles we can infer that the shearing conditions developed in the microchannel, for both Δt periods, appear sufficiently high to keep RBC aggregation at low levels. Published values on RBC aggregation kinetics in shear flow appear to vary with some studies reporting the onset of disaggregation for healthy human RBCs at $\dot{\gamma}$=2.5 s^{-1} [67], whereas others between $\dot{\gamma}$ ~ 70 s^{-1} and 150 s^{-1} [65]. In the present work, the measured shear rates seem to fall within the latter range; the smallest range was observed for WB case which is the most viscous and aggregative sample, with values ranging from $\bar{\bar{\dot{\gamma}}}_{ch}$ is ~ 90s^{-1} at Δt_1 decreasing to ~ 60s^{-1} at Δt_2. Also, for the overall duration of the flow (Δt_3), the average shear values $\bar{\bar{\dot{\gamma}}}_{ch}$, are within the abovementioned disaggregation shear rates. The shear rate profiles provided in Figure 9, suggest that the local blood viscosity in the channel will also be affected. This can be assessed by utilising appropriate viscosity models, as in previous studies[68].

The in- and out-of-plane components of shear ($\frac{d\bar{V}_{ch}}{dx}$ and $\frac{\bar{V}_{ch\,max}}{h}$ respectively) are found to be approximately in the same order of magnitude. An estimation for two specific samples, shows that in the case of WB the mean value of the in-plane component is approximately 10 s^{-1} and the out-of-plane component of shear approximately 70 s^{-1}. For a non-aggregating sample (NAB45%) the mean value of the in-plane component is approximately 16 s^{-1} and the out-of-plane component 100 s^{-1}.

The initial shearing conditions near the entrance of the channel will influence the aggregation state of the samples in the area, which consequently may affect the rheological properties of the samples downstream (shearing history). Figure 10 illustrates the shear behaviour in the flow as calculated from the meniscus velocity. Very high shear rates are observed at the beginning of the flow (> 400 s^{-1}), which decrease, as the flow decelerates, to approximately 100 s^{-1} until about L_m ~ 5mm. The rate of decrease of the shear rate after L_m, until the meniscus reaches the end of the channel (L=20mm) appears low, with moderate shearing conditions in relation to reported disaggregation shear rates ($\bar{\bar{\gamma}}_m$ ~ 50s^{-1}).

When considering the larger meniscus velocities in the initial part of the channel (Figure 6a) and the calculated shear rates $\bar{\dot{\gamma}}_m(z)$ in Figure 10a, it is obvious that intense shearing (>100 s^{-1}) occurs for a significant part of the flow. For the WB case shear rates larger than 300s^{-1} are observed at the beginning of the flow with much larger values for the other samples. This suggests that intense disaggregation takes place at the initial stages of the flow and may continue for the largest portion of the flow for the normal samples. Further, Figure 10b indicates that in general the shearing level that the samples are exposed, are within the abovementioned disaggregation shear rates. The exact shear rate values are subject to errors due to the assumptions made and the velocity measurements and hence should be treated with caution.

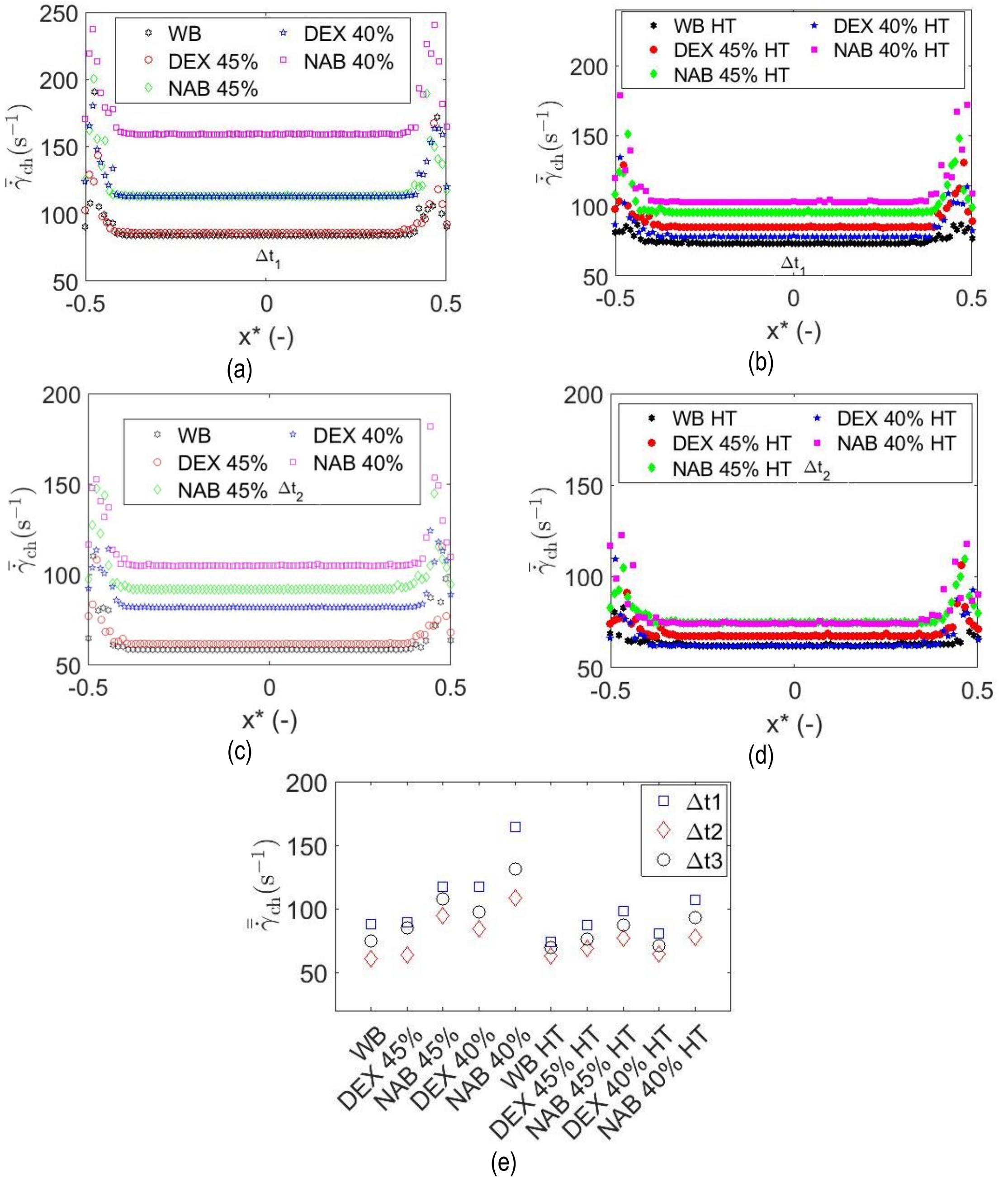

Figure 9. (a) and (b): $\bar{\dot{\gamma}}_{ch}$ at Δt$_1$ for normal and heat-treated samples. (c) and (d): $\bar{\dot{\gamma}}_{ch}$ at Δt$_2$ for normal and heat-treated samples. The mean shear values $\bar{\bar{\dot{\gamma}}}_{ch}$ for Δt$_1$, Δt$_2$ and Δt$_3$ are shown in (e).

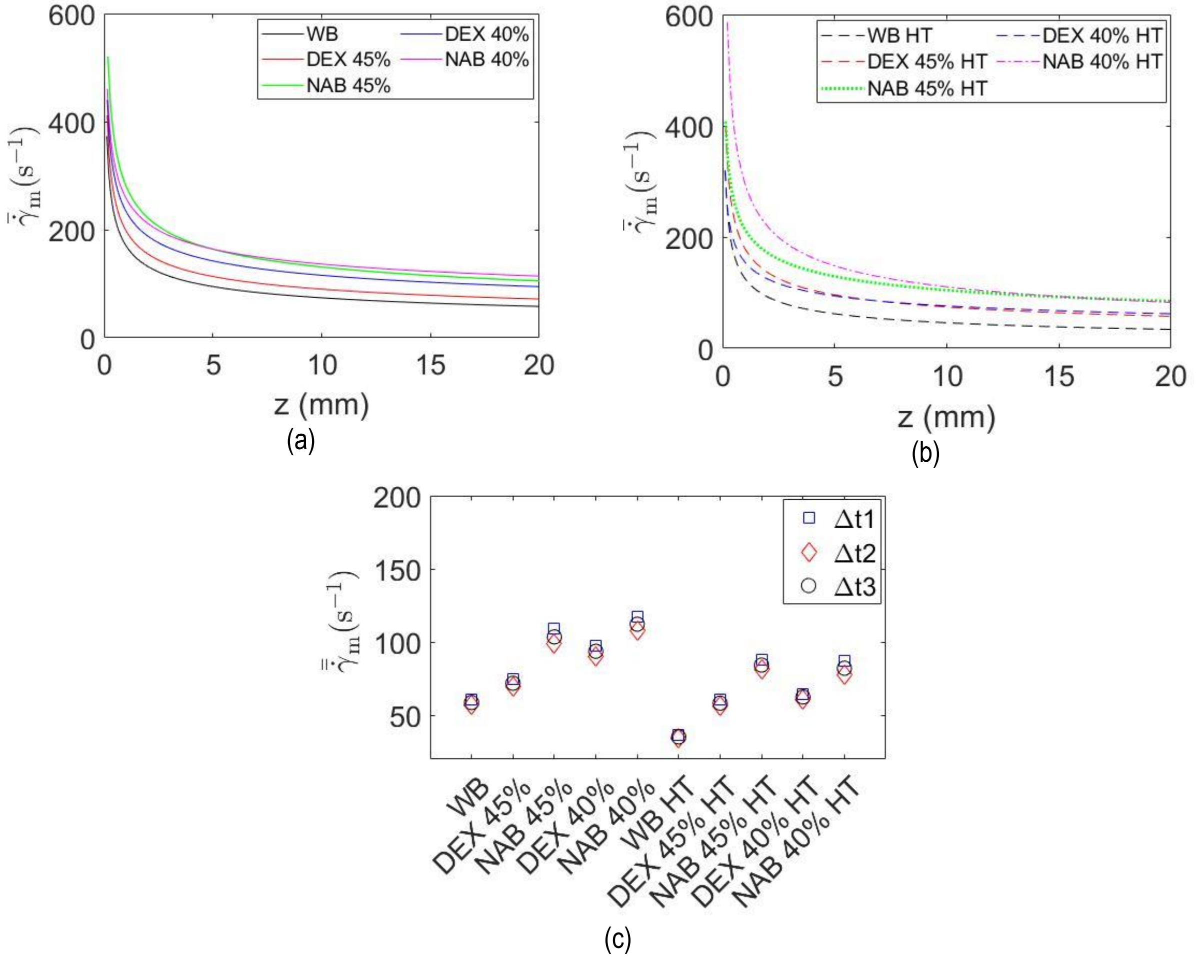

(a)

(b)

(c)

Figure 10. (a): $\bar{\dot{\gamma}}_m$ for all the normal samples, (b): $\bar{\dot{\gamma}}_m$ for all the heat-treated samples, and (c): $\bar{\bar{\dot{\gamma}}}_m$ for the three time periods Δt_1, Δt_2 and Δt_3.

4 Discussion

Several treatment approaches were examined in the present study to increase hydrophilicity, and therefore optimize, the flow conditions in the channel. These included UV exposure (for 10, 20 and 30 mins), plasma treatment (for 5,10,20 and 30 s), TiO_2 coating, and the combination of the aforementioned treatments. The most effective combination, in terms of contact angle and aging time, was plasma treatment for 10s followed by TiO_2 coating. Contact angle initially reduced from ~45° to ~5° after treatment and increased to ~8° within 24 hours (Figure 2). The channels (Figure 3) were manufactured using xurography techniques for the cutting of the channel boundaries, followed by sandwiching the cut double sided adhesive tape between the treated glass slides. This approach ensured the rapid and low-cost production of the test chips.

The increased hydrophilicity of the channel surfaces had a favourable impact on the flow, as seen in the flow of the WB sample for example. For the particular case the mean velocity increased from approximately 2 mm s^{-1} (observed in a similar, untreated, geometry in our previous work[45]) to approximately 8 mms^{-1} (an approximately 4-fold increase) in the present experiments (Figure 4b at z = 10 mm). Part of this increase however, is attributed to the convergent geometry of the channels adopted in this work, compared to the straight configuration used in Pasias *et al.*,[45]. Indeed, it was found that the velocity of the Newtonian fluids tested were higher in the convergent section compared to the straight one in agreement with previous works[9,10].

The influence of rheological parameters in the flow of blood is relatively well understood, and a plethora of works exists in the literature for pressure-driven flows. Much less is known for surface tension driven flows of blood; reports in the literature present mostly information on the velocity of the meniscus, and in certain cases, the local velocity field [7,8,14,16,23,45], with little reference to the hemorheological factors. The present work confirmed that the increased haematocrit, elevates the viscosity of the fluid (Figures 1c and d), in both aggregative and non-aggregative cases, and in the normal and the heat-treated conditions also. This results in smaller channel and meniscus velocities, according to Figures 6 and 7, for both normal and heat-treated samples.

RBC aggregation (RBCA) was measured in the aggregating working fluids (WB and DEX samples), and was found higher in WB samples, since the Dextran concentrations used in the experiments resulted in a moderate aggregation intensity (Figure 5). The most aggregative samples produced a higher apparent viscosity (Figure 5c and d)[64], resulting in reduced mean meniscus and channel velocities (Figures 6 and 7) as expected. RBC deformability was found similar in both aggregative and non-aggregative working fluids, within the normal and the heat-treated sample groups.

As already mentioned the sample handling, and the medium fluids (PBS, and Dextran solutions) do not seem to have a significant effect on the cell deformability. The heat-treatment, however, reduced significantly the cell deformability for all working fluids tested (Figure 5b). The decrease in RBC deformability in the HT samples results in an increase in the viscosity; this is illustrated in the bulk viscosity index $\bar{\bar{\mu}}$ graph in Figures 5c. This is in agreement with other studies in the literature[46,69–75] and results in a decreased mean meniscus and channel velocities (Figures 6b and 7). The heat-treatment of the samples (in particular in the case of WB) could also relate to the direct effects of thermal injuries on blood physiology, and the consequences this may have on the circulatory flow. The importance and role of blood flow in the thermal injury (e.g. heat stroke or exposure to extremely high temperatures) is well documented in the literature[57]. This includes the transport of heat from the body core to the skin surface, and a great increase in cutaneous blood flow. Nevertheless, experimental studies of thermally exposed blood flow in the microscale are scarce in the literature (see for example a study on thermal effects on RBC aggregation in a microchannel flow[76]), and little is known about the local flow characteristics in these cases. The present results suggest a significant influence of the heat effect, not only on blood physiology, but in the local flow characteristics (bulk velocity magnitude and profile).

The aforementioned observations are also reflected in the relations between the hemorheological parameters with the mean meniscus velocity (Figure 11). As expected the most consistent (negative) trend is this of the viscosity on the mean velocity of the fluid in the channel (Figure 11a). For the specific velocity range examined in this work, a linear correlation of the sample viscosity and the mean velocity index was examined, which has an R-Square value of 0.85 and a linearity expressed as $\bar{\bar{\bar{V}}}_m$=-1.13 $\bar{\bar{\mu}}$ + 17.1. For a wider meniscus velocity range however, the non-linear (shear thinning) characteristic of the viscosity behaviour should be more apparent, since the meniscus velocity of the fluid is directly related to the effective shear $\bar{\dot{\gamma}}_m$ (Figure 10) and to the out of plane shear component of $\bar{\dot{\gamma}}_{ch}$ (Figure 9). The impact of the reduced deformability is also apparent between the normal and the heat-treated samples (Figure 11b), whereas the effect of the haematocrit is not very clear when examined explicitly (Figure 11d), mostly due to the relatively narrow haematocrit range (40 – 45%). The aggregation intensity in the samples appears to have a non-monotonic effect on the meniscus velocity; it seems to promote the flow in the heat-treated samples, whereas the opposite is apparent in the normal samples (Figure 11c). For the former, aggregation is very low in the heat-treated samples due to RBC hardening, whereas in the latter case normal aggregation appears for the physiological WB sample and decreased in the Dextran cases. From the trends illustrated in Figure 11, this of the viscosity and velocity (Figure 11c) seems the most consistent, with a correlation found to be -0.92 having an R^2 value of 0.85.

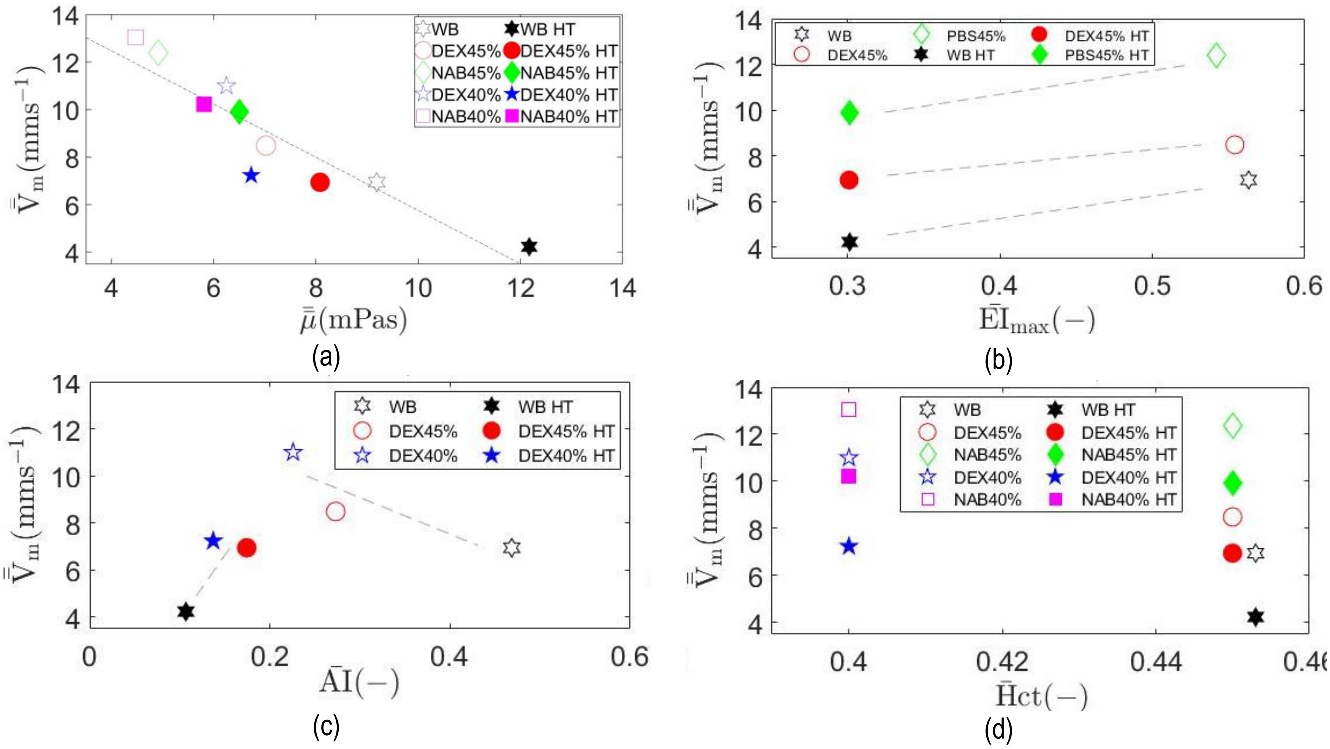

Figure 11. Correlation between velocity and bulk viscosity (a). Trends for deformability index $\bar{\mathrm{EI}}_{\max}$ (b), RBC aggregation index $\overline{\mathrm{AI}}$ (c), and haematocrit (d), with the velocity of the meniscus (lines are not fitted on the data).

When examining the local velocity characteristics (Figure 7) it appears that the heat-treated samples exhibit a higher V_{RI} index, which implies less blunted velocity profiles (Figure 8), similarly to those observed in Passos *et al.*,[39], where the flow of hardened RBCs was examined in straight microchannel pressure driven flows. The bluntness of the profile relates to the local shearing conditions, and can be exploited in microfluidic applications requiring separation of components, as shear gradients are known to affect blood cell transport[77]. The highest V_{RI} index is observed for the normal aggregative DEX40% sample, whereas the largest difference in the V_{RI} between normal and heat-treated samples is obviously in the WB sample. Another important result stemming out from the velocity analysis is the shear characteristics in the channel. High enough shear rates are observed during the flow (Figures 9 and 10) which should cause intense disaggregation conditions in the channel. For the WB case shear rates larger than 300s^{-1} are observed at the beginning of the flow with much larger values for the other samples. Moreover, the values of $\bar{\bar{\gamma}}_m$ in Figure 10b indicate that the overall shearing exposure is above 50 s^{-1}. The moderately elevated shearing conditions observed, could aid the shear-induced mixing (although the effect is rather small[78]) required in microfluidic applications for blood involving reagents,

The favourable flow and shearing conditions developed in the current configuration are also of particular importance for the measurement of hemorheological parameters such as the RBC aggregation intensity. The initial conditions for such measurements require the blood sample to be at dispersed state. Commercial aggregometers (including the Rheoscan-A200 used in the present study) utilise mechanical techniques to achieve the disaggregated state, whereas in the present configuration this is achieved in a passive manner. Hence the developed channel can be potentially used to measure RBCA, using a very small volume of blood (similar to volume produced by finger prick), and by utilising image processing algorithms, similarly to previous works [45].

5 Conclusions

The present study investigated the surface tension driven flow of blood in a superhydrophilic rectangular microchannel with a slightly converging geometry. The influence of RBC aggregation, deformability and haematocrit, and consequently the sample viscosity, on the flow were examined using microPIV and image processing techniques. The study was motivated by the popularity of the particular flow mechanism for point of care diagnostics, and the lack of a systematic approach to assess the effect of important rheological characteristics of blood on the flow performance of such microfluidic set ups.

The treatment of the microchannel surfaces with $Ti0_2$ in combination with the 3-degree convergent channel, significantly improved the flow conditions compared to previous studies in similar geometries. The more aggregative samples were found to have smaller meniscus and channel core velocities than the non-aggregative ones, due to their higher viscosity. The reduced RBC deformability in the heat-treated samples also decreased the velocity of the samples, despite a reduction in the extent of aggregation with heat treatment; an increase in viscosity was also observed in these cases. The haematocrit was also found to have an effect as expected; increasing the haematocrit decreased the velocity of the samples which can be attributed to the higher viscosity of denser samples. No significant variation was observed in the velocity profile characteristics between the normal and heat-treated samples, with the exception of WB, which showed a notable decrease in the V_{RI} index following heat treatment.

Very high shear rates were observed upon initialization of the flow suggesting high disaggregation in the inlet sections of the geometry. The shear rate gradually decreases as the flow proceeds; however, it remains sufficiently high until the flow reaches the end of the channel. The shear conditions developed in the microchannel, especially close to the walls appear sufficiently strong to keep RBC aggregation at low levels for the duration of the flow.

The results of the present study provide important information regarding the surface-tension driven blood flow in converging microchannels with rectangular cross-section, which could aid the design of relevant devices and experiments. Future work should address issues regarding cell distribution and sedimentation, as well as flow extension and duration.

Supplementary Material

See supplementary material for a description of the μPIV validation study.

Acknowledgments

This work was co-funded by the European Regional Development Fund and the Republic of Cyprus through the Research and Innovation Foundation (ref.: EXCELLENCE /0918/0215). The study has also been supported by funding from the internal Start-Up Grants of the Cyprus University of Technology, and by a grant from the and by funding from the Youth Board of Cyprus (Dimitris Pasias scholarship). The authors thank Dr. P. Keivanides for his help on the microchannel surface treatment procedures.

References

1. Sackmann, E. K., Fulton, A. L. & Beebe, D. J. The present and future role of microfluidics in biomedical research. *Nature* **507**, 181–189 (2014).
2. Weigl, B., Domingo, G., Labarre, P. & Gerlach, J. Towards non- and minimally instrumented, microfluidics-based diagnostic devices. *Lab Chip* **8**, 1999–2014 (2008).
3. Tsui, J. H., Lee, W., Pun, S. H., Kim, J. & Kim, D. H. Microfluidics-assisted in vitro drug screening and carrier production. *Advanced Drug Delivery Reviews* vol. 65 1575–1588 (2013).
4. Berthier, E. & Beebe, D. J. Flow rate analysis of a surface tension driven passive micropump. *Lab Chip* **7**, 1475–8 (2007).
5. Zhong, Q., Ding, H., Gao, B., He, Z. & Gu, Z. Advances of Microfluidics in Biomedical Engineering. *Advanced Materials Technologies* vol. 4 (2019).
6. Chang, C. K., Lai, C. C. & Chung, C. K. Numerical analysis and experiments of capillarity-driven microfluid chip. in *NEMS 2011 - 6th IEEE International Conference on Nano/Micro Engineered and Molecular Systems* (2011). doi:10.1109/NEMS.2011.6017532.
7. Kung, C. F., Chiu, C. F., Chen, C. F., Chang, C. C. & Chu, C. C. Blood flow driven by surface tension in a microchannel. *Microfluid. Nanofluidics* **6**, 693–697 (2009).
8. Berthier, J. *et al.* Whole blood spontaneous capillary flow in narrow V-groove microchannels. *Sensors Actuators, B Chem.* **206**, 258–267 (2015).

9. Erickson, D., Li, D. & Park, C. B. Numerical simulations of capillary-driven flows in nonuniform cross-sectional capillaries. *J. Colloid Interface Sci.* (2002) doi:10.1006/jcis.2002.8361.
10. Saha, A. A., Mitra, S. K., Tweedie, M., Roy, S. & McLaughlin, J. Experimental and numerical investigation of capillary flow in SU8 and PDMS microchannels with integrated pillars. *Microfluid. Nanofluidics* **7**, 451–465 (2009).
11. Chen, Y. F. *et al.* Surface tension driven flow for open microchannels with different turning angles. *Microfluid. Nanofluidics* **5**, 193–203 (2008).
12. Ichikawa, N., Hosokawa, K. & Maeda, R. Interface motion of capillary-driven flow in rectangular microchannel. *J. Colloid Interface Sci.* **280**, 155–164 (2004).
13. Berthier, J. *et al.* On the halt of spontaneous capillary flows in diverging open channels. *Med. Eng. Phys.* (2017) doi:10.1016/j.medengphy.2017.05.005.
14. Berthier, J. *et al.* Spontaneous capillary flow in curved, open microchannels. *Microfluid. Nanofluidics* (2016) doi:10.1007/s10404-016-1766-6.
15. Lee, J. J., Berthier, J., Theberge, A. B. & Berthier, E. Capillary Flow in Open Microgrooves: Bifurcations and Networks. *Langmuir* **35**, (2019).
16. Gosselin, D. *et al.* Viscoelastic capillary flow: The case of whole blood. *AIMS Biophys.* (2016) doi:10.3934/biophy.2016.3.340.
17. Jun, W., Wei, H., Raghbir S., B. & Pin, T. Modeling of Surface-Tension-Driven Flow of Blood in Capillary Tubes. *Tech Sci. Press* **1**, 161–167 (2004).
18. Cherry, E. M. & Eaton, J. K. Shear thinning effects on blood flow in straight and curved tubes. *Phys. Fluids* **25**, 73104 (2013).
19. Kubochkin, N. & Gambaryan-Roisman, T. Surface force-mediated dynamics of droplets spreading over wetting films. *Phys. Fluids* **33**, 122107 (2021).
20. Lei, J., Xu, Z., Xin, F. & Lu, T. J. Dynamics of capillary flow in an undulated tube. *Phys. Fluids* **33**, (2021).
21. Wang, Y., Nunna, B. B., Talukder, N., Etienne, E. E. & Lee, E. S. Blood plasma self-separation technologies during the self-driven flow in microfluidic platforms. *Bioengineering* vol. 8 (2021).
22. Sakamoto, H., Hatsuda, R., Miyamura, K. & Sugiyama, S. Plasma separation PMMA device driven by capillary force controlling surface wettability. *Micro Nano Lett.* (2012) doi:10.1049/mnl.2011.0627.
23. Sneha Maria, M., Rakesh, P. E., Chandra, T. S. & Sen, A. K. Capillary flow of blood in a microchannel with differential wetting for blood plasma separation and on-chip glucose detection. *Biomicrofluidics* **10**, (2017).
24. Chang, Y. J., Lin, Y. Te & Liao, C. C. Chamfer-Type Capillary Stop Valve and Its Microfluidic Application to Blood Typing Tests. *SLAS Technol.* **24**, (2019).
25. Dunne, P. *et al.* Liquid flow and control without solid walls. *Nature* **581**, (2020).
26. Lima, R., Wada, S., Takeda, M., Tsubota, K. ichi & Yamaguchi, T. In vitro confocal micro-PIV measurements of blood flow in a square microchannel: The effect of the haematocrit on instantaneous velocity profiles. *J. Biomech.* (2007) doi:10.1016/j.jbiomech.2007.01.012.
27. Lima, R., Wada, S., Tsubota, K. I. & Yamaguchi, T. Confocal micro-PIV measurements of three-dimensional profiles of cell suspension flow in a square microchannel. *Meas. Sci. Technol.* **17**, 797–808 (2006).
28. Lima, R. *et al.* Radial dispersion of red blood cells in blood flowing through glass capillaries: The role of hematocrit and geometry. *J. Biomech.* **41**, 2188–2196 (2008).
29. Sherwood, J. M., Dusting, J., Kaliviotis, E. & Balabani, S. The effect of red blood cell aggregation on velocity and cell-depleted layer characteristics of blood in a bifurcating microchannel. *Biomicrofluidics* (2012) doi:10.1063/1.4717755.
30. Sherwood, J. M. J. M., Kaliviotis, E., Dusting, J. & Balabani, S. Hematocrit, viscosity and velocity distributions of aggregating and non-aggregating blood in a bifurcating microchannel. *Biomech. Model. Mechanobiol.* **13**, 259–273 (2014).
31. Sherwood, J. M. J. M., Holmes, D., Kaliviotis, E. & Balabani, S. Spatial distributions of red blood cells significantly alter local haemodynamics. *PLoS One* **9**, (2014).

32. Kaliviotis, E., Pasias, D., Sherwood, J. M. & Balabani, S. Red blood cell aggregate flux in a bifurcating microchannel. *Med. Eng. Phys.* (2017) doi:10.1016/j.medengphy.2017.04.007.
33. Kaliviotis, E., Sherwood, J. M. & Balabani, S. Partitioning of red blood cell aggregates in bifurcating microscale flows. *Sci. Rep.* (2017) doi:10.1038/srep44563.
34. Kaliviotis, E., Sherwood, J. M. & Balabani, S. Local viscosity distribution in bifurcating microfluidic blood flows. *Phys. Fluids* **30**, (2018).
35. Haque, M. E., Matin, A., Wang, X. & Kersaudy-Kerhoas, M. Effects of syringe pump fluctuations on cell-free layer in hydrodynamic separation microfluidic devices. *Phys. Fluids* **33**, (2021).
36. Reinhart, W. H., Piety, N. Z. & Shevkoplyas, S. S. Influence of red blood cell aggregation on perfusion of an artificial microvascular network. *Microcirculation* DOI: 10.1111/micc.12317 (2016) doi:10.1111/micc.12317.
37. Mehri, R., Laplante, J., Mavriplis, C. & Fenech, M. Investigation of blood flow analysis and red blood cell aggregation. *J. Med. Biol. Eng.* **34**, 469–474 (2014).
38. Mehri, R., Mavriplis, C. & Fenech, M. Red blood cell aggregates and their effect on non-Newtonian blood viscosity at low hematocrit in a two-fluid low shear rate microfluidic system. *PLoS One* (2018) doi:10.1371/journal.pone.0199911.
39. Passos, A. *et al.* The effect of deformability on the microscale flow behavior of red blood cell suspensions. *Phys. Fluids* (2019) doi:10.1063/1.5111189.
40. Czaja, B. *et al.* The influence of red blood cell deformability on hematocrit profiles and platelet margination. *PLoS Comput. Biol.* (2020) doi:10.1371/journal.pcbi.1007716.
41. Alam, A. U., Howlader, M. M. R. & Deen, M. J. The effects of oxygen plasma and humidity on surface roughness, water contact angle and hardness of silicon, silicon dioxide and glass. *J. Micromechanics Microengineering* (2014) doi:10.1088/0960-1317/24/3/035010.
42. Luo, S. & Wong, C. P. Effect of UV/ozone treatment on surface tension and adhesion in electronic packaging. *IEEE Trans. Components Packag. Technol.* (2001) doi:10.1109/6144.910801.
43. Topala, I., Dumitrascu, N. & Pohoata, V. Influence of plasma treatments on the hemocompatibility of PET and PET + TiO 2 films. *Plasma Chem. Plasma Process.* (2008) doi:10.1007/s11090-008-9136-0.
44. Kim, Hwa-Min, Sung Bo Seo, Dong Young Kim, Kang Bae, and S. Y. S. Enhanced Hydrophilic Property of TiO2 Thin Film Deposited on Glass Etched with O2 Plasma. *Trans. Electr. Electron. Mater.* **14**, 152–155 (2013).
45. Pasias, D., Passos, A., Constantinides, G., Balabani, S. & Kaliviotis, E. Surface tension driven flow of blood in a rectangular microfluidic channel: Effect of erythrocyte aggregation. *Phys. Fluids* **32**, (2020).
46. Xue, S., Lee, B. K. & Shin, S. Disaggregating shear stress: The roles of cell deformability and fibrinogen concentration. *Clin. Hemorheol. Microcirc.* (2013) doi:10.3233/CH-2012-1627.
47. Baskurt, O. K. *et al.* Comparison of three instruments for measuring red blood cell aggregation. *Clin. Hemorheol. Microcirc.* **43**, 283–298 (2009).
48. Baskurt, O. K. *et al.* Comparison of three commercially available ektacytometers with different shearing geometries. *Biorheology* (2009) doi:10.3233/BIR-2009-0536.
49. Horobin, J. T., Sabapathy, S. & Simmonds, M. J. Red blood cell tolerance to shear stress above and below the subhemolytic threshold. *Biomech. Model. Mechanobiol.* **19**, 851–860 (2020).
50. Gillissen, J. J. J., Papadopoulou, A., Balabani, S., Tiwari, M. K. & Wilson, H. J. Suspension rheology of adhesive particles at high shear-rates. *Phys. Rev. Fluids* (2020) doi:10.1103/PhysRevFluids.5.053302.
51. La Notte, L. *et al.* Airbrush spray coating of amorphous titanium dioxide for inverted polymer solar cells. *Int. J. Photoenergy* (2012) doi:10.1155/2012/897595.
52. Suciu, R. C. *et al.* TiO2 thin films prepared by spin coating technique. in *Revue Roumaine de Chimie* (2011).
53. Bartholomeusz, D. A., Boutté, R. W. & Andrade, J. D. Xurography: Rapid prototyping of microstructures using a cutting plotter. *J. Microelectromechanical Syst.* (2005) doi:10.1109/JMEMS.2005.859087.
54. Szekely, J., Neumann, A. W. & Chuang, Y. K. The rate of capillary penetration and the applicability of the washburn equation. *J. Colloid Interface Sci.* (1971) doi:10.1016/0021-9797(71)90120-2.

55. Kuok, K. K. & Chiu, P. C. Application of Particle Image Velocimetry (PIV) for Measuring Water Velocity in Laboratory Sedimentation Tank. *IRA-International J. Technol. Eng. (ISSN 2455-4480)* **9**, 16 (2017).

56. Poelma, C., Kloosterman, A., Hierck, B. P. & Westerweel, J. Accurate Blood Flow Measurements: Are Artificial Tracers Necessary? *PLoS One* **7**, (2012).

57. Bouchama, A. *et al.* Classic and exertional heatstroke. *Nat. Rev. Dis. Prim.* **8**, (2022).

58. Nilsson, A. M., Lucassen, G. W., Verkruysse, W., Andersson-Engels, S. & van Gemert, M. J. C. <title>Optical properties of human whole blood: changes due to slow heating</title>. in *Laser-Tissue Interaction and Tissue Optics II* vol. 2923 24–34 (SPIE, 1996).

59. Amin, M., Hussain, M. A., Shahwar, D. & Hussain, M. *Thermal Analysis and Degradation Kinetics of Dextran and Highly Substituted Dextran Acetates*. *J.Chem.Soc.Pak* vol. 37 (2015).

60. Masuelli, M. A. Dextrans in Aqueous Solution. Experimental Review on Intrinsic Viscosity Measurements and Temperature Effect. *J. Polym. Biopolym. Phys. Chem.* **1**, 13–21 (2013).

61. Chien, S. & Jan, K. Ultrastructural basis of the mechanism of rouleaux formation. *Microvasc. Res.* **5**, 155–166 (1973).

62. Kitamura, H. *et al.* Roles of hematocrit and fibrinogen in red cell aggregation determined by ultrasonic scattering properties. *Ultrasound Med. Biol.* (1995) doi:10.1016/0301-5629(95)00022-J.

63. Lerche, D. & Baumler, H. Moderate heat treatment of only red blood cells (RBC) slows down the rate of RBC-RBC aggregation in plasma. *Biorheology* (1984) doi:10.3233/BIR-1984-21308.

64. Merrill, E. W., Gilliland, E. R., Lee, T. S. & Salzman, E. W. Blood rheology: effect of fibrinogen deduced by addition. *Circ. Res.* (1966) doi:10.1161/01.RES.18.4.437.

65. Snabre, P., Bitbol, M. & Mills, P. Cell disaggregation behavior in shear flow. *Biophys. J.* **51**, 795–807 (1987).

66. Dupire, J., Socol, M. & Viallat, A. Full dynamics of a red blood cell in shear flow. *Proc. Natl. Acad. Sci. U. S. A.* (2012) doi:10.1073/pnas.1210236109.

67. Firsov, N. N., Priezzhev, A. V. & Ryaboshapka, O. M. Study of erythrocyte-aggregation kinetics in shear flow in vitro by light-scattering technique. in *Proceedings of SPIE - The International Society for Optical Engineering* vol. 1981 (1993).

68. Kaliviotis, E., Sherwood, J. M. M. & Balabani, S. Local viscosity distribution in bifurcating microfluidic blood flows. *Phys. Fluids* **30**, (2018).

69. Rakow, A. L. & Hochmuth, R. M. Effect of heat treatment on the elasticity of human erythrocyte membrane. *Biophys. J.* **15**, 1095–1100 (1975).

70. Nash, G. B. & Meiselman, H. J. Alteration of red cell membrane viscoelasticity by heat treatment: Effect on cell deformability and suspension viscosity. *Biorheology* **22**, 73–84 (1985).

71. Sammartano, A., Scarlattei, M., Migliari, S., Baldari, G. & Ruffini, L. Validation of in vitro labeling method for human use of heat-damage red blood cells to detect splenic tissue and hemocateretic function. *Acta Biomed.* **90**, 275–280 (2019).

72. Yoshino, M. & Murakami, K. A kinetic study of the inhibition of yeast AMP deaminase by polyphosphate. *Biochim. Biophys. Acta - Protein Struct. Mol. Enzymol.* **954**, 271–276 (1988).

73. Atkins, H. L., Goldman, A. G. & Fairchild, R. G. Splenic sequestration of 99mTc labeled, heat treated red blood cells. *Radiology* **136**, 501–503 (1980).

74. Bustamante, C. J., Chemla, Y. R., Liu, S. & Wang, M. D. Optical tweezers in single-molecule biophysics. *Nat. Rev. Methods Prim. 2021 11* **1**, 1–29 (2021).

75. Liu, Z., Li, H. & Qiang, Y. Computational modeling of the biomechanics and biorheology of heated red blood cells Nature-Inspired Hierarchical Advanced Material Design View project Biology of red blood cells View project. *Artic. Biophys. J.* (2021) doi:10.1016/j.bpj.2021.09.038.

76. Seidner, H., Gunter, G., Weber-Fishkin, S. & Frame, M. Erythrocyte Aggregation in Hyperthermic Hypoxic Conditions Significantly Related to Self-identified Race. *FASEB* **35**, (2021).

77. Zhou, J. *et al.* Isolation of cells from whole blood using shear-induced diffusion. *Sci. Rep.* **8**, (2018).

78. Lopez, M. & Graham, M. D. Enhancement of mixing and adsorption in microfluidic devices by shear-induced diffusion and topography-induced secondary flow. *Phys. Fluids* **20**, (2008).

Author Contributions

E.K. and S.B. designed the study, and oversee and contributed on the analysis of the data. D.P. performed the experimental work, analysed the data and developed the manuscript. G.C. and L.K contributed on the surface treatment of the microchannels. A.P. contributed on the analysis of the data. All authors contributed in the writing of the manuscript.

Additional Information:

Ethics Approval

The study has been approved by the Cyprus Bioethics Committee (ref: ΕΕΒΚ/ΕΠ/2016/18).

Competing Interests Statement

The authors declare no competing financial or other interests.

Data availability

Data, subject to ethical restrictions, are available on request from the authors.

FIGURE 1

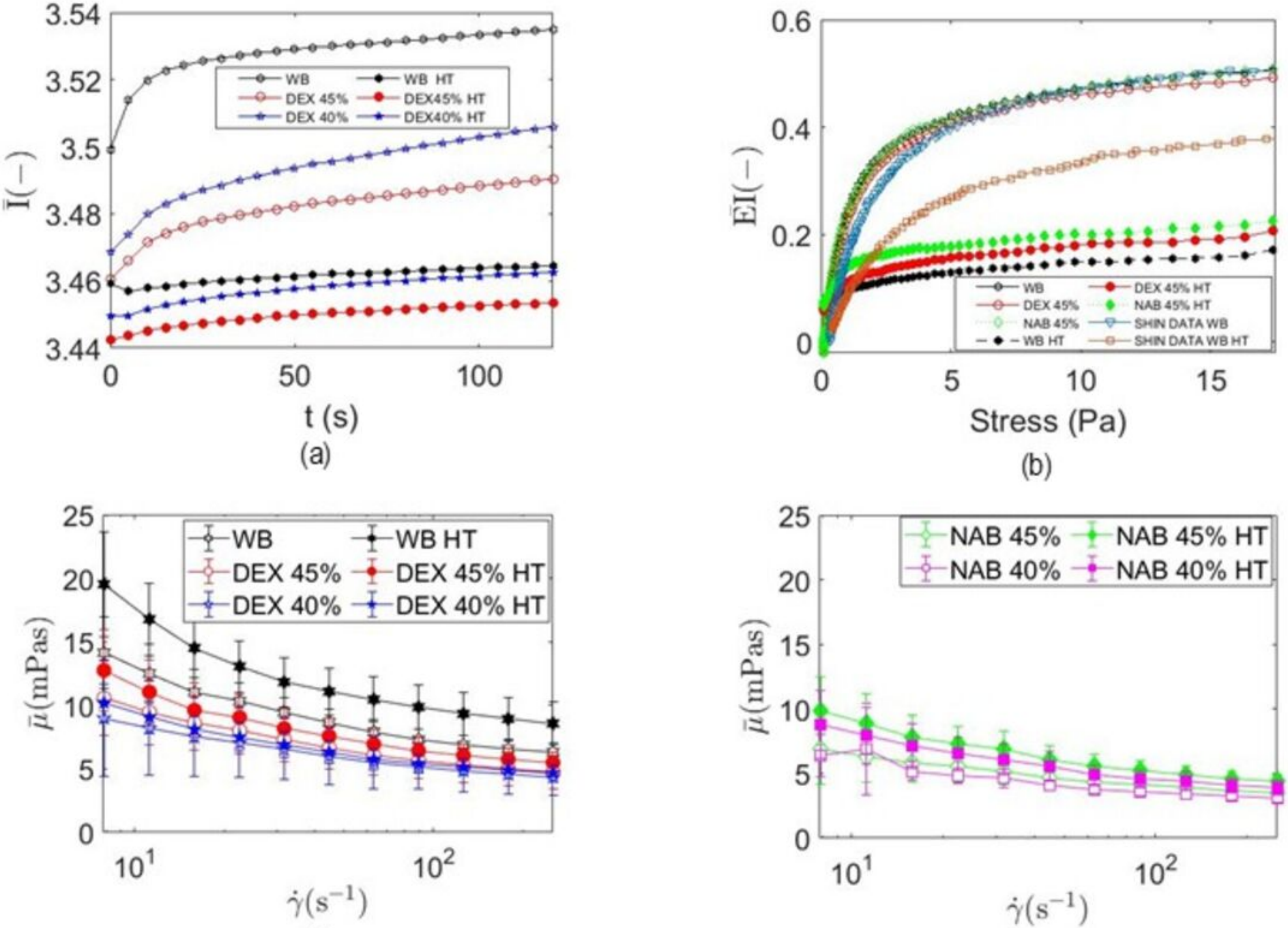

(a)

(b)

(c)

(d)

FIGURE 2

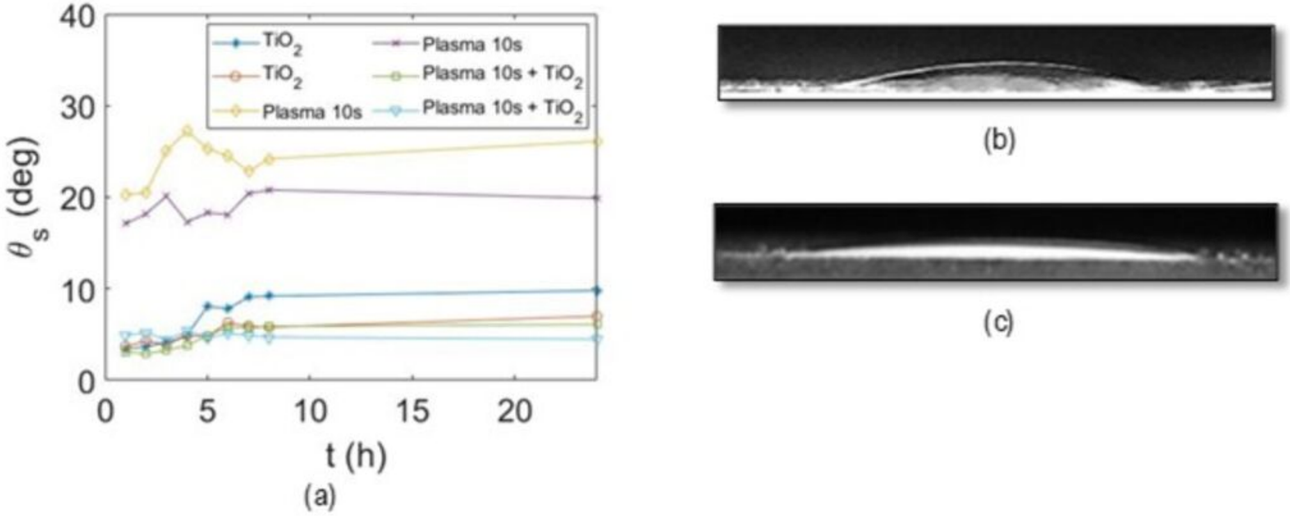
40
30
20
10
0
θ_s (deg)
0
5
10
15
20
t (h)
TiO$_2$
TiO$_2$
Plasma 10s
Plasma 10s
Plasma 10s + TiO$_2$
Plasma 10s + TiO$_2$

(a)

(b)

(c)

FIGURE 3

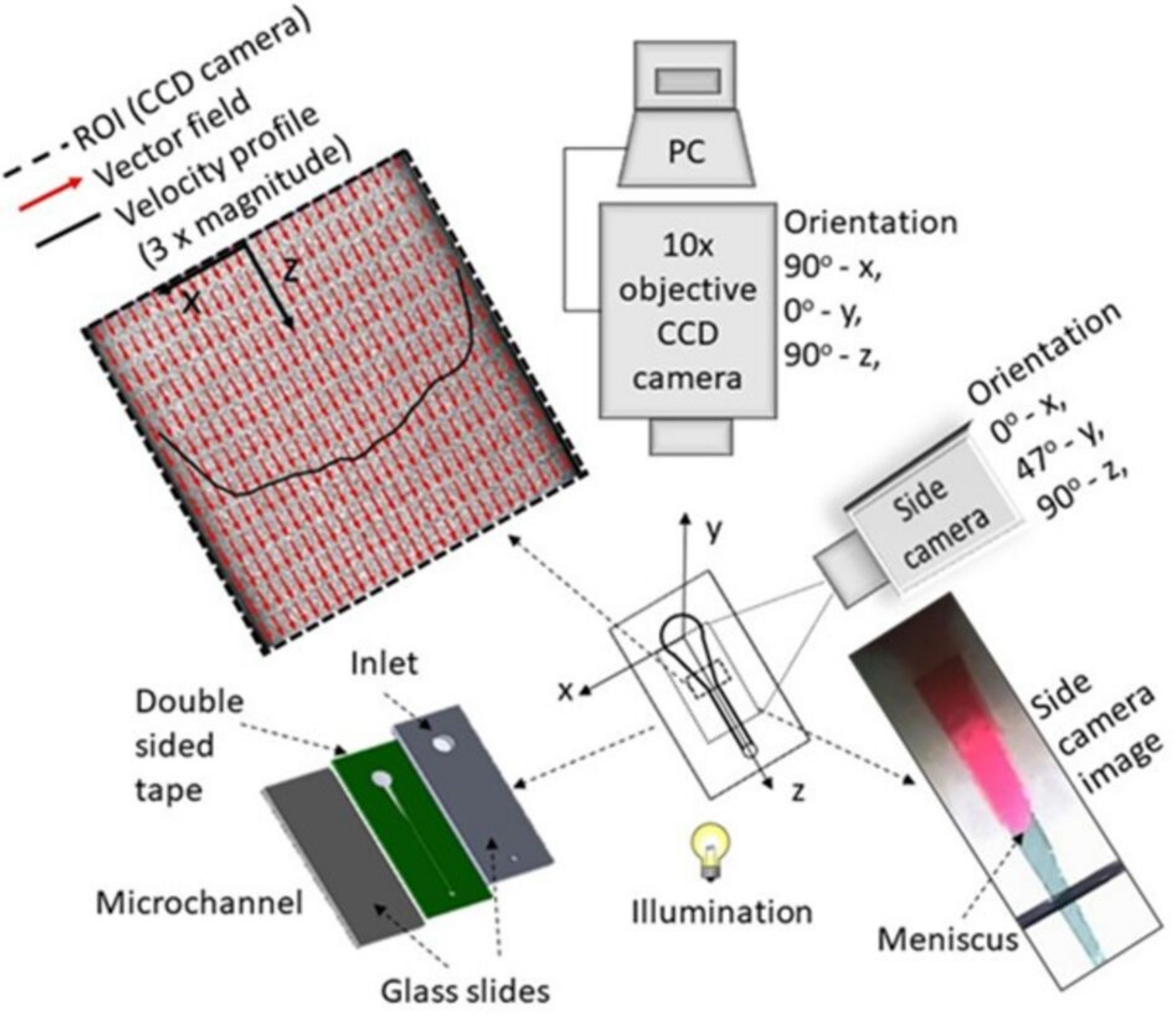
ROI (CCD camera)
Vector field
Velocity profile
(3 x magnitude)
x
z
PC
10x objective CCD camera
Orientation
90° - x,
0° - y,
90° - z,
Orientation
0° - x,
47° - y,
90° - z,
Side camera
y
x
z
Inlet
Double sided tape
Microchannel
Glass slides
Illumination
Side camera image
Meniscus

FIGURE 4

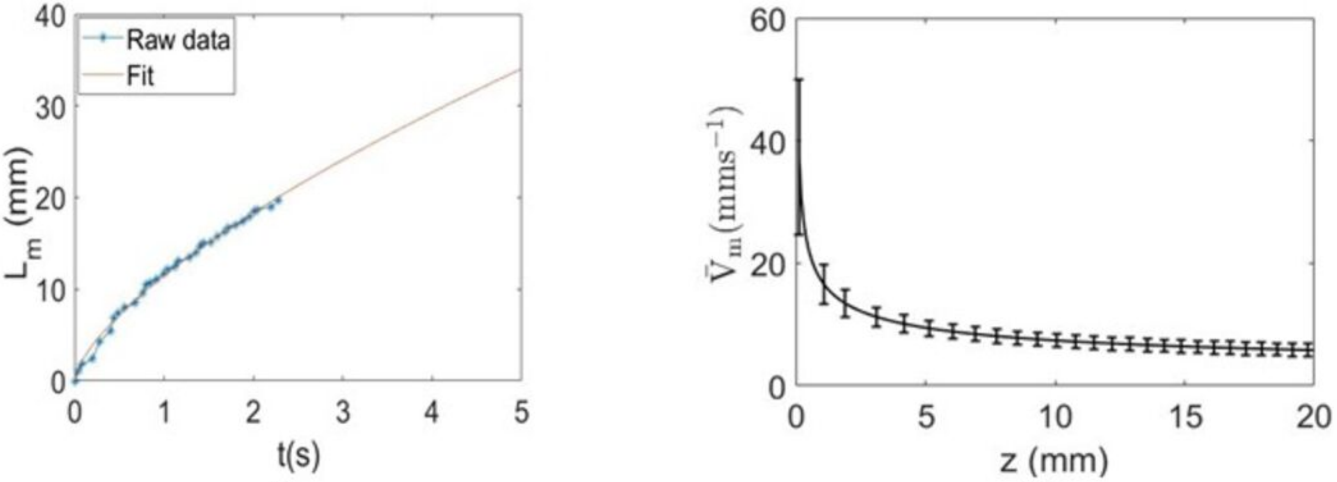
Raw data
Fit
L_m (mm)
t(s)
0
10
20
30
40
0
1
2
3
4
5
$\bar{V}_m(\mathrm{mms}^{-1})$
z (mm)
0
20
40
60
0
5
10
15
20

(a)

(b)

FIGURE 5

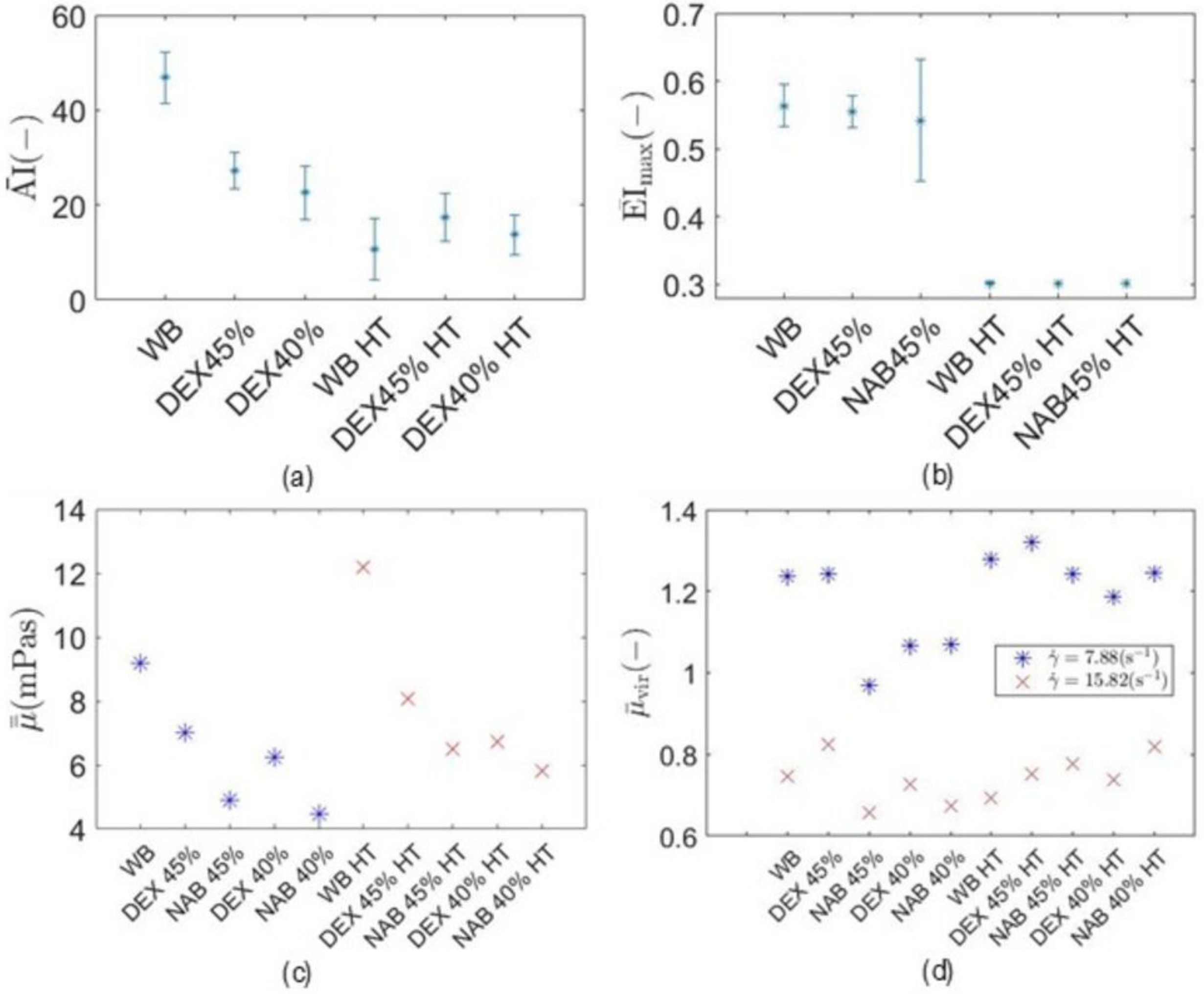

(a)

(b)

(c)

(d)

FIGURE 6

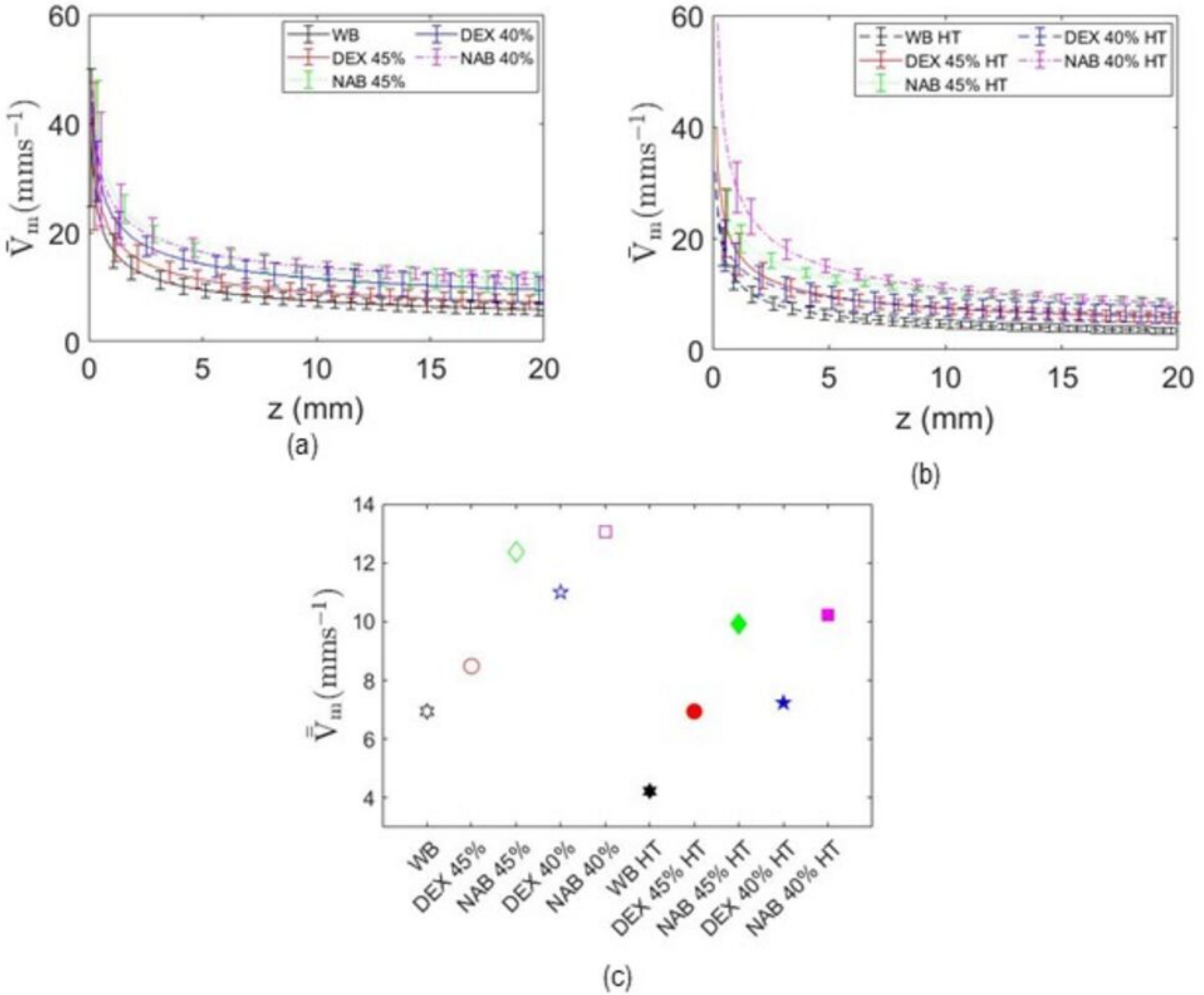
60
40
20
0
$\bar{V}_m(\mathrm{mms}^{-1})$
WB
DEX 45%
NAB 45%
DEX 40%
NAB 40%
0
5
10
15
20
z (mm)
60
40
20
0
$\bar{V}_m(\mathrm{mms}^{-1})$
WB HT
DEX 45% HT
NAB 45% HT
DEX 40% HT
NAB 40% HT
0
5
10
15
20
z (mm)
14
12
10
8
6
4
$\bar{\bar{V}}_m(\mathrm{mms}^{-1})$
WB
DEX 45%
NAB 45%
DEX 40%
NAB 40%
WB HT
DEX 45% HT
NAB 45% HT
DEX 40% HT
NAB 40% HT

(a)

(b)

(c)

FIGURE 7

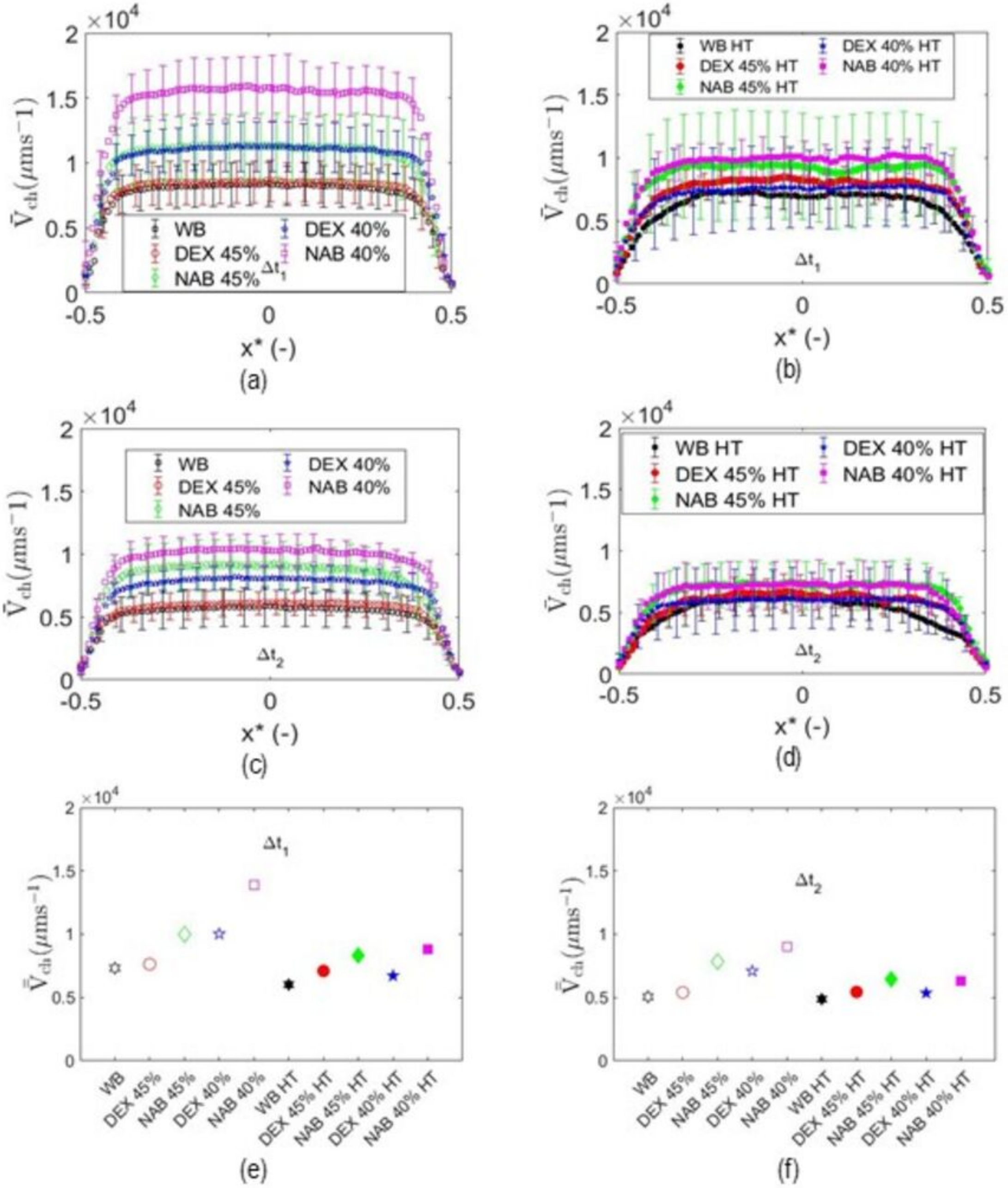
×10^4
2
1.5
1
0.5
0
$\bar{V}_{ch}(\mu ms^{-1})$
-0.5
0
0.5
x* (-)
WB
DEX 45%
NAB 45%
DEX 40%
NAB 40%
Δt1
(a)
WB HT
DEX 45% HT
NAB 45% HT
DEX 40% HT
NAB 40% HT
Δt1
(b)
Δt2
(c)
Δt2
(d)
Δt1
WB
DEX 45%
NAB 45%
DEX 40%
NAB 40%
WB HT
DEX 45% HT
NAB 45% HT
DEX 40% HT
NAB 40% HT
(e)
Δt2
(f)

FIGURE 8

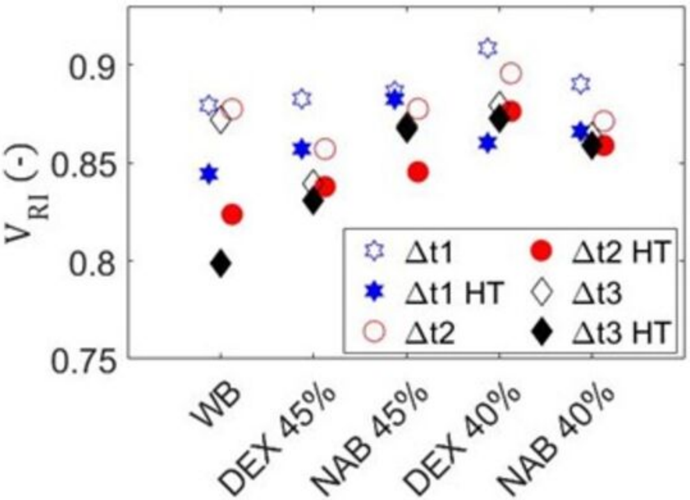
V_{RI} (-)
0.9
0.85
0.8
0.75
WB
DEX 45%
NAB 45%
DEX 40%
NAB 40%
Δt1
Δt1 HT
Δt2
Δt2 HT
Δt3
Δt3 HT

FIGURE 9

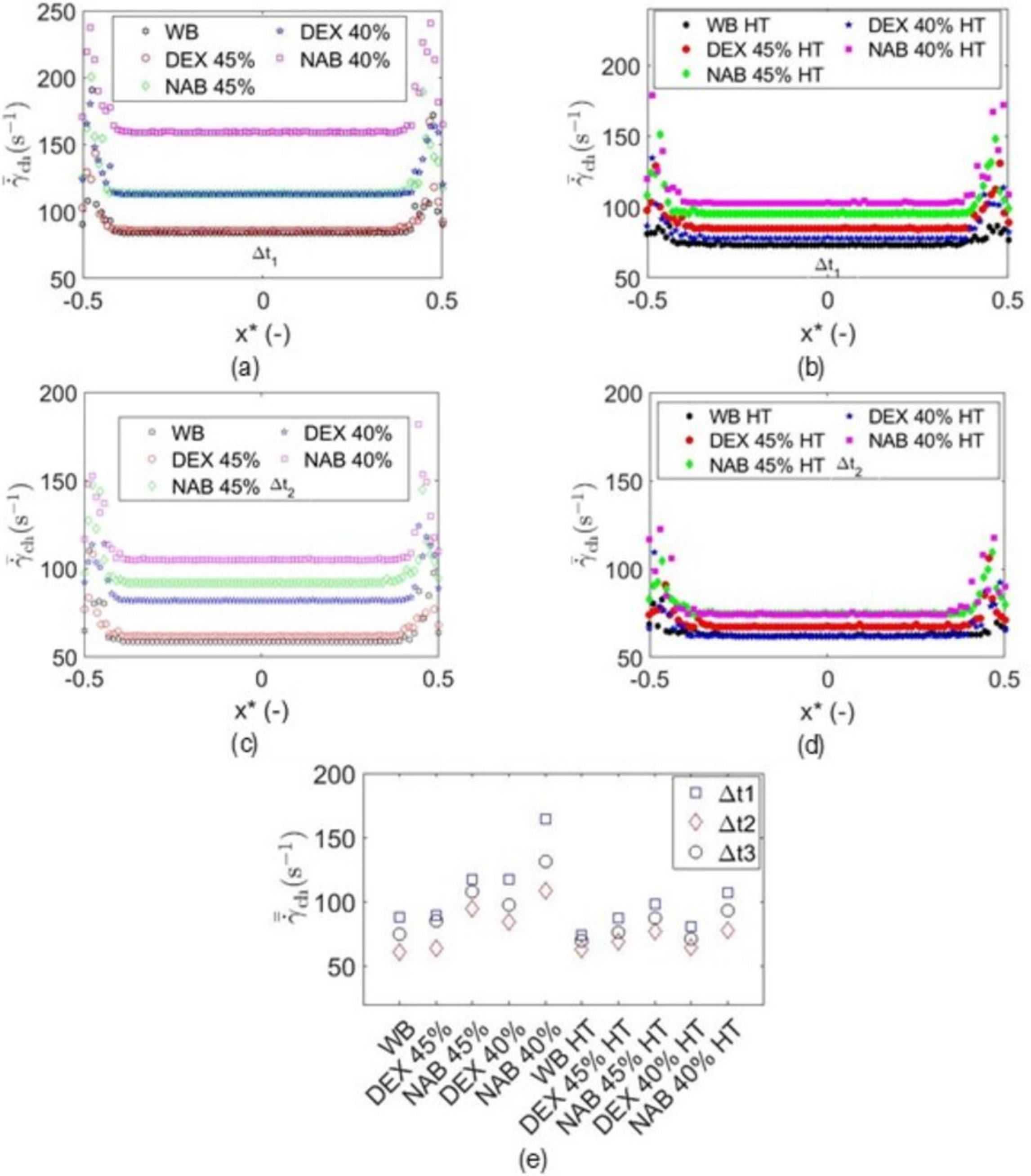
250
200
150
100
50
$\bar{\dot{\gamma}}_{\mathrm{ch}}(\mathrm{s}^{-1})$
WB
DEX 45%
NAB 45%
DEX 40%
NAB 40%
Δt_1
-0.5
0
0.5
x* (-)
(a)
WB HT
DEX 45% HT
NAB 45% HT
DEX 40% HT
NAB 40% HT
Δt_1
(b)
WB
DEX 45%
NAB 45%
DEX 40%
NAB 40%
Δt_2
(c)
WB HT
DEX 45% HT
NAB 45% HT
DEX 40% HT
NAB 40% HT
Δt_2
(d)
$\bar{\bar{\dot{\gamma}}}_{\mathrm{ch}}(\mathrm{s}^{-1})$
Δt1
Δt2
Δt3
WB
DEX 45%
NAB 45%
DEX 40%
NAB 40%
WB HT
DEX 45% HT
NAB 45% HT
DEX 40% HT
NAB 40% HT
(e)

FIGURE 10

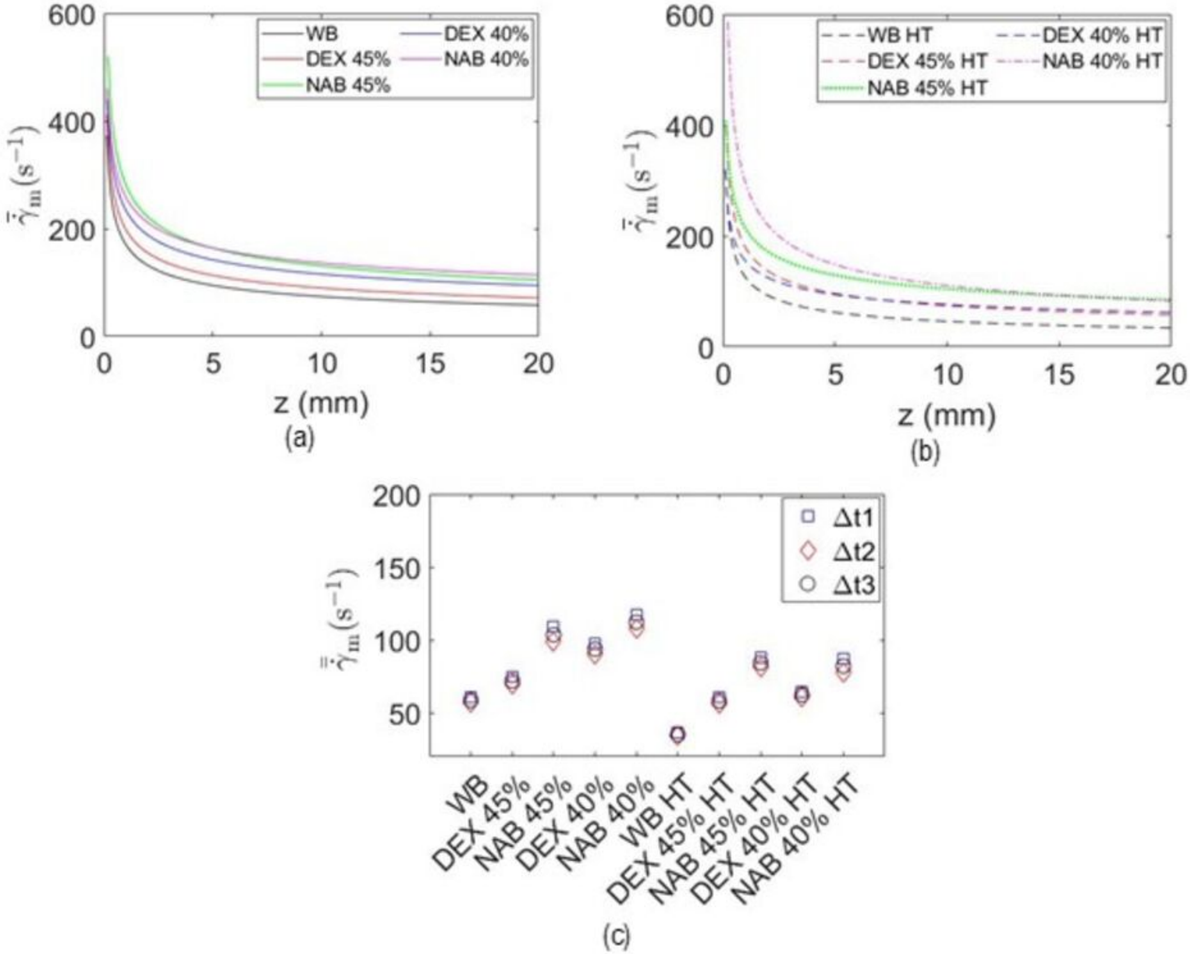

(a)

(b)

(c)

FIGURE 11

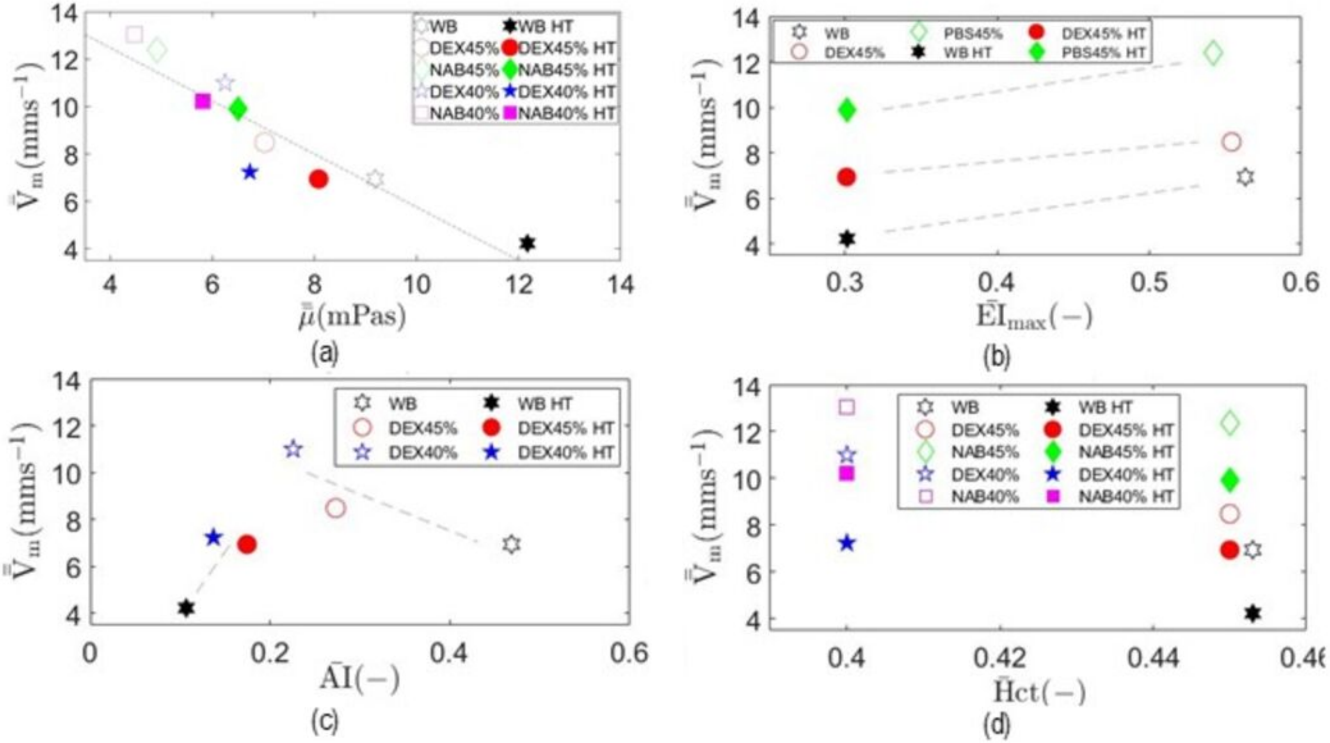
(a)
$\bar{\bar{V}}_m(mms^{-1})$
$\bar{\bar{\mu}}(mPas)$
14
12
10
8
6
4
4
6
8
10
12
14
WB
WB HT
DEX45%
DEX45% HT
NAB45%
NAB45% HT
DEX40%
DEX40% HT
NAB40%
NAB40% HT
(b)
$\bar{\bar{V}}_m(mms^{-1})$
$\bar{\bar{EI}}_{max}(-)$
14
12
10
8
6
4
0.3
0.4
0.5
0.6
WB
DEX45%
PBS45%
WB HT
DEX45% HT
PBS45% HT
(c)
$\bar{\bar{V}}_m(mms^{-1})$
$\bar{\bar{AI}}(-)$
14
12
10
8
6
4
0
0.2
0.4
0.6
WB
WB HT
DEX45%
DEX45% HT
DEX40%
DEX40% HT
(d)
$\bar{\bar{V}}_m(mms^{-1})$
$\bar{\bar{Hct}}(-)$
14
12
10
8
6
4
0.4
0.42
0.44
0.4
WB
WB HT
DEX45%
DEX45% HT
NAB45%
NAB45% HT
DEX40%
DEX40% HT
NAB40%
NAB40% HT